

Extreme Solar Particle Storms

The hostile Sun

Edited by

Fusa Miyake

Ilya Usoskin

Stepan Poluianov

An American Astronomical Society and IOP Publishing partnership



Extreme Solar Particle Storms

The hostile Sun

Fusa Miyake, Ilya Usoskin and Stepan Poluianov

Chapter 6

Characterization of the Measured Events

E Cliver, Y Ebihara, H Hayakawa, T Jull, F Mekhaldi, F Miyake and R Muscheler

In this chapter, we summarize the characterization of known extreme solar events.

The lack of signatures of the directly known large solar events, including GLEs in the mid-20th century and the Carrington event, in cosmogenic records is discussed in Section 6.1. Compelling evidence that the cosmogenic-based events of 774/775 CE, 993/994 CE and 660 BCE originated in extreme SEP events is presented. The principal evidence for a solar origin is the well-documented hemispheric symmetry, with latitudinal dependence, of the observed signal for ^{10}Be , ^{36}Cl , and ^{14}C . At present, the cosmogenic-isotope-defined SEP events—the 775 CE event in particular—provide the best evidence that the Sun is capable of producing superflares with energies up to 10^{33} erg. This allows cosmogenic-based SEP events to be used as global high-precision time markers (isochrones).

The deduction of historical SEP spectra using the $^{36}\text{Cl}/^{10}\text{Be}$ ratio is presented in Section 6.2. All three historical cosmogenic SEP events were shown to have hard spectra. Use of the $^{36}\text{Cl}/^{10}\text{Be}$ ratio is a particularly promising approach to look for large soft-spectra events in conjunction with magnetic storms and aurorae.

The revitalization of historical magnetic and auroral studies are reviewed in Section 6.3. Such studies have provided additional documentation for the 19th and 20th century storms (e.g., 1872 and 1921)—indicating their equivalence with the well-known 1859 event—and let us reconstruct the equatorward boundary of the auroral oval, rather than just that of auroral visibility. This approach lets us further discuss the storm intensity on the basis of its correlation with the equatorward boundary of the auroral oval and contextualize the extreme event in 1859, not as a unique event but one of the most extreme space weather events after the mid-19th century.

The possibility that special conditions are needed to produce a cosmogenic SEP event is shown in Section 6.4. Such events may require a combination of solar circumstances (e.g., both a very large flare and a background of energetic seed particles from previous eruptions) for a detectable ^{10}Be or ^{14}C signature. It is argued

that the event of 774/775 CE may conservatively serve as the worst-case scenario for extreme SEP events on the timescale of 10^4 years.

6.1 Observed SEP events: Knowns and Unknowns

FUSA MIYAKE, A. J. TIMOTHY JULL, AND HISASHI HAYAKAWA

6.1.1 Introduction

As discussed in Section 4.2, energetic particles take part in nuclear reactions with atmospheric atoms, and in the course of these reactions, many types of secondary particles are produced, including cosmogenic isotopes such as ^{14}C , ^{10}Be , ^{36}Cl , etc. Because SEP events typically occur on a very short timescale of hours to days, they should be detectable as rapid (≤ 1 year) excursions in cosmogenic isotope concentrations in high-resolution measurements of tree rings and ice cores. Accordingly, cosmogenic isotopes can serve as proxies for past SEP events (Lingenfelter & Ramaty 1970; Usoskin et al. 2006; Webber et al. 2007). The first detection of such a rapid excursion in cosmogenic nuclides was reported in 2012, as a single-year excursion in ^{14}C concentrations detected in tree rings dendrochronologically dated to 774–775 CE (Miyake et al. 2012). An extreme SEP event is considered the most plausible origin of the 775 CE excursion. The discovery of the 775 CE event led to the accumulation of high-precision and high-time-resolution (one to two years) ^{14}C concentration data in tree rings. From such high-resolution data, several rapid ^{14}C excursions were reported: the 775 CE, 993/994 CE, 660 BCE, and 3371 BCE events (e.g., Miyake et al. 2013; Park et al. 2017; Wang et al. 2017; O’Hare et al. 2019). In addition, high-resolution ^{10}Be and ^{36}Cl concentration data from ice cores have been measured (e.g., Mekhaldi et al. 2015). The measured concentrations of these cosmogenic isotopes and their ratios have been used to contextualize the causes of cosmic-ray events (Section 6.2). On the other hand, none of the SEP events known from direct observations was accompanied by clearly measurable excursions in cosmogenic isotope concentrations. In this chapter, we give an overview of rapid-increase events as detected or undetected in cosmogenic isotope data.

6.1.2 Proxy Data for Extreme SEP Events

Cosmogenic Isotopes

We have already discussed in Section 4.2 how solar energetic particles (SEPs) can produce cosmogenic nuclides in the atmosphere. However, how strong should the SEP event be in order to produce a measurable amount of nuclides? Would these nuclide excursions be expected to be of a detectable magnitude given the current measurement precision? Here, we first show whether the recorded SEP events are accompanied by significant excursions in actual measured cosmogenic isotope data. In order to search for SEP-related cosmogenic isotope data, it would be better to select events during the space age, as we have direct information on them during this time period. However, because of anthropogenic nuclear pollution, related mostly to nuclear-bomb tests after the 1950s, subsequent isotope (^{14}C , ^{36}Cl , ^3H) variations of natural origin have become very difficult to discern at least until the late 1970s (for

^{36}Cl and ^3H). As a case in point, a large increase in cosmogenic isotope concentrations was observed after the late 1950s. Atmospheric ^{14}C concentrations, for example, rapidly increased by approximately 100% from 1963 to 1964 (Hua & Barbetti 2014). This large excursion in cosmogenic isotopes occurred because of atmospheric nuclear tests and is called the “bomb effect” (Section 7.1.1). Therefore, we focus on the data before the 1960s to minimize the anthropogenic influence on these cosmogenic isotopes.

Table 6.1 shows the main recorded events before 1960. Most of them are ground-level enhancements (GLEs—see Section 2.2), which are SEP events observed by ground-based detectors as sudden increases in the count rate. Here, we introduce cosmogenic isotope data for the dates corresponding to the recorded GLEs as the most reliable record of SEP events in this time interval. Figure 6.1 depicts the ^{14}C concentration data corresponding to the period 1870 through 1954 (Stuiver et al. 1998b) and from 1955 to 1956 (Hua & Barbetti 2014). No distinct ^{14}C peaks appeared corresponding to the observed GLEs in 1942, 1946, and 1949. The first nuclear test occurred in 1945, but it was not until 1955–1956 (Hua & Barbetti 2014) that the global average $\Delta^{14}\text{C}$ data clearly showed a rapid and substantial increase due to the bomb effect. The rapid ^{14}C increase after the late 1950s occurred because of nuclear tests, and it is difficult to assess GLEs #5–7 using ^{14}C data.

For the period from 1870 to 1954, one can observe gradual variations but no rapid ^{14}C excursion events. Thus, significant excursions in ^{14}C concentrations failed to appear in connection with not only the recorded GLEs, but also any unknown extreme SEP events that might have occurred during that period. The decreasing trend from the 1900s to the 1950s can be explained by the Suess effect (Suess 1955), which is a dilution effect due to anthropogenic carbon released from fossil fuel burning.

On the other hand, a possible link between several SEP events and the annual ^{10}Be data was reported by McCracken & Beer (2015). Using annual ^{10}Be data obtained from two Greenland ice cores (Dye 3 and the North Greenland Ice-core Project, NGRIP), they found some peaks that might be related to GLEs #1, #4, and #5, as well as to some major geomagnetic storms prior to 1938. They showed that ^{10}Be peaks appeared one to three years after the occurrence of the GLE or magnetic

Table 6.1. Strongest Solar Events for the Period 1859 through 1959, including the Carrington event and GLEs

Date (CE)	Name
1859 September 1–2	Carrington event
1942 February 28	GLE #1
1942 March 7	GLE #2
1946 July 25	GLE #3
1949 November 19	GLE #4
1956 February 23	GLE #5

Note. GLEs #1–4 were detected using ionization chambers, events after 1951 were recorded by neutron monitors.

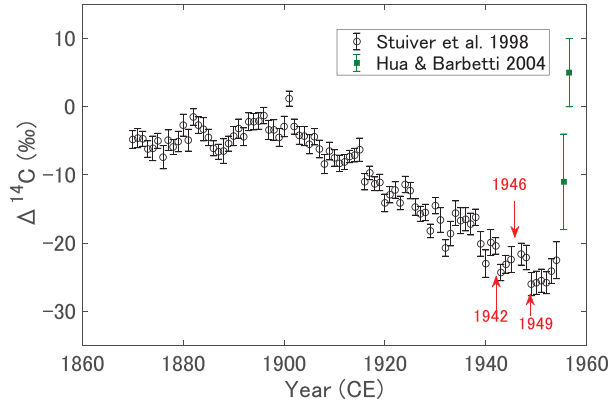


Figure 6.1. Annual ^{14}C data for the period from 1870 to 1954 obtained from tree-ring measurements (Stuiver et al. 1998b); global average annual ^{14}C data for 1955.5 and 1956.5 from several ^{14}C data sets (Hua & Barbetti 2014). The arrows indicate years of GLEs #1–4. No significant ^{14}C excursion has been reported for the period from 1870 to 1954, including the GLEs.

storm and explained this lag by means of the ^{10}Be deposition process (McCracken & Beer 2015). On the other hand, Pedro et al. (2009) have shown that there might be some ^{10}Be peaks in the Law Dome Summit high-resolution Antarctic data set, related to strong GLEs, but they are hardly recognizable over the noisy background. Compared with ^{14}C concentrations, which are homogenized by the global carbon cycle, ^{10}Be concentrations in ice cores are understood to reflect more direct information regarding variations in cosmic rays (Chapter 4). Therefore, it is possible that the ^{10}Be data show a higher sensitivity to extreme SEP events than ^{14}C data do. While ^{10}Be data contain more direct information regarding cosmic-ray variations, they are also disturbed by other causes occurring during deposition (climate changes and volcanic eruptions; see Baroni et al. 2011 and Sections 4.3 and 7.1). Because there are few data sets of quasi-annual ^{10}Be concentrations, SEP-event candidate ^{10}Be signals need to be confirmed through additional verification using several ice cores and by comparing ^{10}Be records with other proxies such as the sulfate concentration to identify volcanic disturbances for instance.

The first solar flare ever reported, the 1859 September 1 Carrington event (Carrington 1859; Hodgson 1859), is also considered to be the largest flare ever observed (Cliver & Dietrich 2013) on the basis of the associated magnetic crochet (Stewart 1861; Cliver & Svalgaard 2004), although the SEP scale for the 1859 event is unsettled. Accordingly, data for several cosmogenic isotopes have been collected around the years of the Carrington event. Figure 6.2 shows annual data for ^{14}C concentrations, namely, those of Stuiver et al. (1998b) and Miyake et al. (2013). While Stuiver et al. used the Douglas fir sample from the Olympic Peninsula in the US, Miyake et al. used Japanese cedar samples from Yaku Island in Japan. Despite the mutual consistency of the two ^{14}C series within the measurement error, neither showed any rapid excursion after 1859. In addition, no signal related to the Carrington event has been found in annually resolved ^{10}Be records (McCracken &

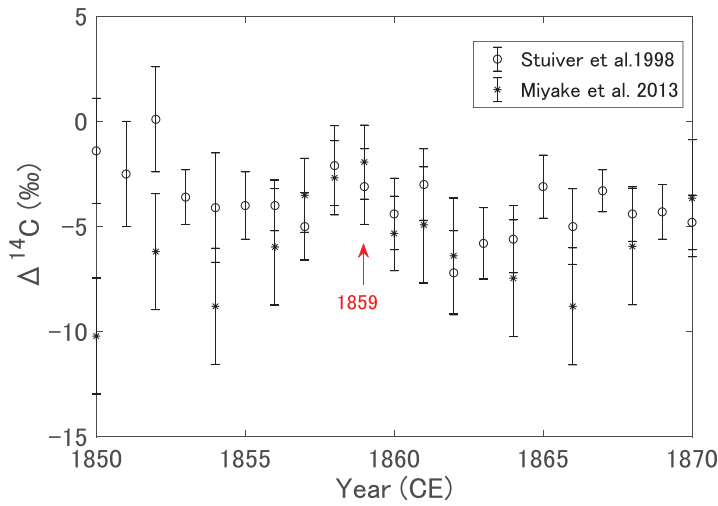


Figure 6.2. Annual ^{14}C data around the Carrington event (Carrington 1859). There is no evident rapid ^{14}C increase around 1859 (cf. Usoskin & Kovaltsov 2012). The two data series are adopted from Stuiver et al. and Miyake et al., who, respectively, used North American Douglas fir and Japanese cedar trees (Stuiver et al. 1998b; Miyake et al. 2013).

Beer 2015; Usoskin & Kovaltsov 2012). Accordingly, we conclude that the Carrington event was incapable of producing a detectable amount of cosmogenic isotopes in measured data.

Nitrate

In the early 2000s, a chemical proxy for strong SEP events was discussed and even applied to assess SEP fluxes over the last five centuries (McCracken et al. 2001). This proxy was based on measurements of nitrate in polar ice cores, in the belief that a fraction of stratospheric nitrate produced via ionization and dissociation processes induced by energetic particles can lead to recognizable peaks in the data. In particular, the largest nitrate spike in the last ~ 400 years was found close in time to the Carrington event.

However, it has been shown in subsequent studies that no distinct nitrate spikes, corresponding to the known SEP events including the Carrington event, can be found in most ice cores from Greenland or Antarctica (Wolff et al. 2008, 2012; Mekhaldi et al. 2017). Moreover, the existing nitrate spikes (including the one close to the Carrington event) in Greenland cores were shown to be caused not by extreme SEP events but by biomass-burning plumes (Wolff et al. 2012). Finally, a theoretical study using climate models showed that even extreme events are not expected to produce nitrate spikes detectable in ice cores (Duderstadt et al. 2016; Sukhodolov et al. 2017). Accordingly, it is clear now that nitrate cannot serve as a proxy for SEP events. Therefore, the scientific reason to associate the Carrington event with the strongest SEP event as in McCracken et al. (2001) has been lost.

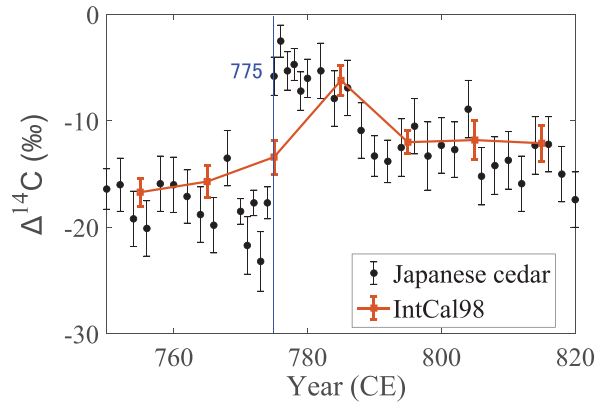


Figure 6.3. Comparison between the decadal IntCal98 data (Stuiver et al. 1998a) and annual Japanese cedar data (Miyake et al. 2012) for the period from 750 to 820 CE.

6.1.3 Data on Events Detected Using Cosmogenic Isotopes

775 CE Event

Although no significant increase in ^{14}C concentrations has been found corresponding to known events in the space era, extremely large SEP events, by far exceeding the directly observed ones, may have occurred in the past and recorded as a rapid increase in ^{14}C concentration. In order to find such rapid increases in ^{14}C concentration, Miyake et al. (2012) focused on the period for which the increase rate in ^{14}C concentration was the largest in low-resolution ^{14}C data, namely, the IntCal ^{14}C calibration curve (Reimer et al. 2013), the time resolution of which is 10 years for the Holocene. If there was a period during which the ^{14}C concentration greatly increased in a short time period, the IntCal data have the best chance of capturing and revealing such sudden changes. Miyake et al. studied the period around 780 CE, when ^{14}C concentration shows the largest increase rate in IntCal data over the Holocene (cf. Usoskin & Kovaltsov 2012), and found a single-year rapid increase in ^{14}C concentration from 774 to 775 CE using annual ^{14}C measurements of Japanese cedar tree samples (Figure 6.3). The ^{14}C increment was a $\sim 12\text{‰}$ increase in 774–775 CE ($\sim 15\text{‰}$ overall in 774–776 CE), which is much larger than a typical 2–3‰ error for ^{14}C data and much larger than the $\leq 1\text{‰}$ normal annual ^{14}C variation. Hereafter, we call this rapid ^{14}C increase the 775 CE event.

Miyake et al. (2012) modeled the measured ^{14}C profile using a simple box model of the carbon cycle. The best-fit value for the ^{14}C production rate due to SEP was found to be $(1.5 \pm 0.3) \times 10^8$ atoms/cm², whereas the best-fit value for the injection time was found to be less than one year (Miyake et al. 2012, 2014). In order to explain the 775 CE event using various carbon-cycle models and other ^{14}C data, subsequent authors estimated the ^{14}C production rate as $(1.3\text{--}2.1) \times 10^8$ atoms/cm² (Usoskin et al. 2013; Pavlov et al. 2013; Gütthler et al. 2015; Mekhaldi et al. 2015; Büntgen et al. 2018). These ^{14}C production rates are approximately two to three times greater than the normal background production rate by galactic cosmic rays.

Following the discovery of the 775 CE event by Miyake et al. (2012), a detailed profile of ^{14}C concentrations during this event was investigated using numerous tree samples from all over the world. From such studies, it became clear that the ^{14}C increment corresponding to the 775 CE event was evident globally (Usoskin et al. 2013; Jull et al. 2014; Gütthler et al. 2015; Rakowski et al. 2015; Park et al. 2017; Uusitalo et al. 2018; Büntgen et al. 2018). Büntgen et al. (2018) issued the most recent report, based on high-precision ^{14}C measurements using tree samples from 34 sites in the southern and northern hemispheres (Figure 6.4). In their averaged northern hemisphere $\Delta^{14}\text{C}$ data, they observed a 4‰ increase in 773–774 CE, an additional 9.5‰ increase in 774–775 CE, and a further 2‰ increase in 775–776 CE. After 776 CE, a gradual decline was observed, as in the aforementioned Japanese cedar result. In the southern hemisphere data, the observed increases were smaller, a 7‰ increase in 774–775 CE, followed by a 6‰ additional increase in 775–776 CE. These profiles of the northern and southern hemispheres were modeled using a detailed carbon-cycle box model with 11 box divisions in each hemisphere (Büntgen et al. 2018). From this carbon-cycle modeling, the date of ^{14}C input was estimated to be July ± 1 month of 774 CE. Meanwhile, Uusitalo et al. (2018) estimated the timing of the same enhancement to be May–June 774 CE, but they suggested that the timing of the solar event itself might be a few months earlier considering uncertainties such as the average atmospheric oxidation time of ^{14}C (one to two months).

When the 775 CE event was discovered, its origin was not well understood. Several phenomena have subsequently been proposed as the possible cause of the 775 CE event: for example, a galactic gamma-ray event such as a nearby supernova (SN) or gamma-ray burst (GRB; Miyake et al. 2012; Hambaryan & Neuhäuser 2013; Pavlov et al. 2013), a cometary collision with Earth (Liu et al. 2014), or an

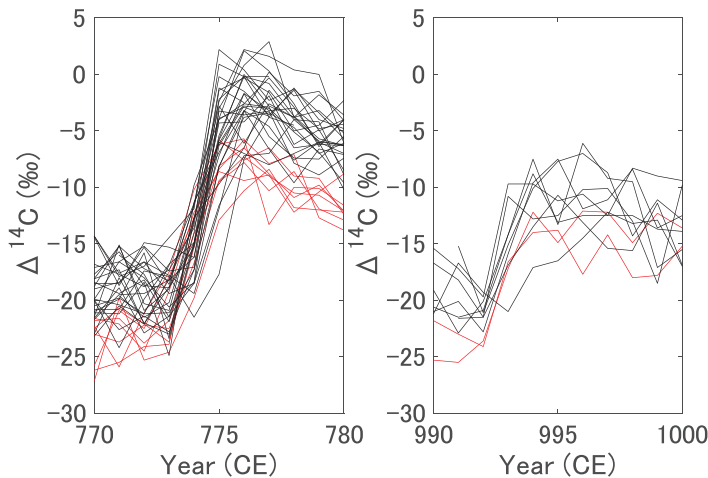


Figure 6.4. Worldwide $\Delta^{14}\text{C}$ data in tree rings for the 775 CE event (left) and the 993/994 CE event (right; Büntgen et al. 2018). The black lines represent the northern hemisphere results, and the red lines represent the southern hemisphere results.

extreme SEP event (Eichler & Mordecai 2012; Melott & Thomas 2012; Miyake et al. 2013; Thomas et al. 2013; Usoskin et al. 2013; Cliver et al. 2014; Güttler et al. 2015; Usoskin & Kovaltsov 2015; Büntgen et al. 2018; Uusitalo et al. 2018). Currently, an extreme SEP event remains the only valid hypothesis for the origin of this event (see details in Section 7.1).

Büntgen et al. (2018) performed a ^{14}C analysis using samples from around the world and showed a latitude dependence in ^{14}C concentrations, which tends to increase with latitude. A similar and indeed significant latitude dependence in ^{14}C data also appears in northern hemisphere tree-sample data during the increase phase of the 775 CE event (Uusitalo et al. 2018). Such a latitude dependence suggests that the event was caused by charged particles affected by the geomagnetic field, thus supporting the SEP origin.

As there was apparently a large cosmic-ray inflow in the year 774–775 CE, it is highly possible that cosmic rays simultaneously generated cosmogenic isotopes other than ^{14}C and that these might be equally detectable in measured data (Usoskin & Kovaltsov 2012). Miyake et al. (2015) measured quasi-annual ^{10}Be concentrations in an ice core from Antarctic Dome Fuji and detected a significant increase in ^{10}Be concentration against background variation close to 775 CE in its ice-core age. Sigl et al. (2015) and Mekhaldi et al. (2015) also measured ^{10}Be concentrations with a resolution of approximately 0.5–1 year using ice cores from Greenland (NEEM, NGRIP, and TUNU2013), and Antarctica (WDC). This work revealed ^{10}Be increases of similar size to that of the Dome Fuji data, again significantly larger than the background variation. Although the estimated dates for these ^{10}Be excursions do not align perfectly with those of 775 CE, it was suggested that they likely represent the same cosmic-ray event, for three reasons. First, the difference from 775 CE is only a few years in ice-core age, which was determined using several independent methods including volcanic tie-point matching (see Section 5.3). Second, the observed ^{10}Be excursions are significantly larger than background variations. Finally, the bipolar symmetry characteristic of worldwide ^{14}C excursions is also observed in quasi-annual ^{10}Be data, indicating a cause like an SEP event that would produce an inflow of cosmic rays equally over both hemispheres. While the 775 CE event is observed in most cosmogenic isotope data as a rapid increase of their single-year concentrations, no significant nitrate spike has been observed in several ice cores from both hemispheres at this time (Sukhodolov et al. 2017; Mekhaldi et al. 2017).

Several estimates of the scale of the event have been made assuming a particular SEP energy spectrum. Assuming that the cosmic-ray input can be scaled with that of GLE #5 (1956 February 23), which had the hardest energy spectrum yet observed during the space age (see Section 2.2), Usoskin et al. (2013) proposed that the 775 CE event would have been a factor of 25–50 stronger than that of the GLE #5. Using a similar approach, Sukhodolov et al. (2017) reproduced the 775 CE event in ^{10}Be data using the chemical-climate model SOCOL. This was confirmed by Mekhaldi et al. (2015), who, using the ratio of different isotopes, showed that the 775 CE event can be explained by an SEP event with a very hard energy spectrum (see Section 6.2).

Alternatively, the absence of ^{14}C excursions corresponding to historically recorded SEP events (Section 6.1) can be used to constrain the 775 CE event size. Assuming that the ^{14}C increase corresponding to the largest observed event (GLE #5) does not exceed the uncertainties in the ^{14}C data (viz. $\sim 1\%$), the 775 CE event should be at least an order of magnitude larger than any event observed during the space era.

Such an extreme SPE could have been caused by a superflare more than ~ 10 times larger than the largest historically observed solar flare. Such superflares have been observed in several solar-type stars in our galaxy, but the direct relation between solar and stellar flares is controversial (see Section 7.3). Because no superflare has been directly observed for our Sun, the 775 CE event serves as a cornerstone for the possibility of solar superflares (see Section 6.4).

Since the discovery of the 775 CE event, many additional measurements and discussions of the causes have taken place, making it the best-studied single-year cosmic-ray increase event. The discovery of the 775 CE event has also prompted annual measurements of ^{14}C concentrations as background to further event surveys.

993/994 CE Event

The second rapid ^{14}C increase dating back to 993–994 CE was discovered in a survey of an extended period from the 7th century CE to the 11th century CE, using the Japanese cedar tree sample (Miyake et al. 2013). This rapid ^{14}C increase was confirmed soon thereafter using the Japanese cypress data set (Miyake et al. 2014). Similar ^{14}C increases were found from early wood of 994 CE to late wood of 994 CE in Danish oak data, as well as in Polish samples (Rakowski et al. 2018). Büntgen et al. (2018) measured ^{14}C concentrations in nine tree samples from both hemispheres and confirmed a rapid increase similar to that observed for the 775 CE event (Figure 6.4). Notably, the year in which the rapid ^{14}C increase occurred differs slightly among the data sets. Measurements using Japanese and Danish tree samples show a clear ^{14}C increase from 993 to 994 CE, whereas most of the ^{14}C increases in the data of Büntgen et al. (2018) occurred from 992 to 993 CE. The estimated event date, therefore, also differs, that is, April–June 994 CE for Danish oak data (Fogtmann-Schulz et al. 1999) and April 993 CE (± 2 months) for the Büntgen et al. (2018) data set. Although the reasons for this disparity are not well understood, it might reflect factors as simple as differences in location of tree species. After all, most of the data show the same rapid ^{14}C increase around 992–994 CE. In future work, there is a need to undertake ^{14}C concentration measurements of higher precision in order to clarify the precise event date.

Existing data suggest that the ^{14}C increase for the 993/994 CE event is nearly half that of the 775 CE event. Figure 6.5 shows a comparison between the 775 and 993/994 CE events, based on averaged northern hemisphere data from Büntgen et al. (2018). The two events show a common pattern: a rapid ^{14}C increase within approximately one year, followed by a gradual attenuation. This similarity further confirms a common cause for the two events (i.e., a short-term inflow of cosmic rays).

As in the case of the 775 CE event, the 993/994 CE event's cause could be ascribed to an extreme SEP event or a GRB, but the present paradigm is that it was caused by

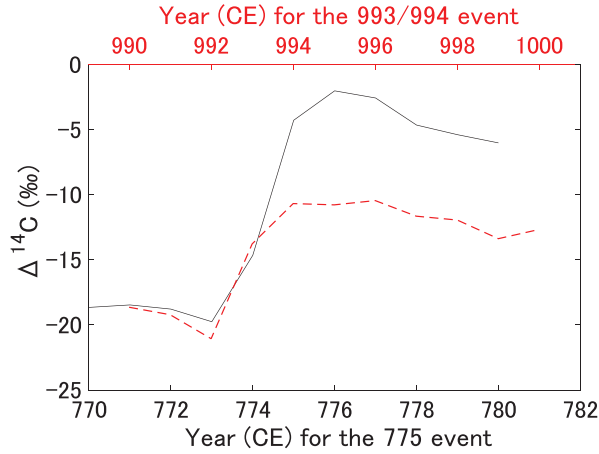


Figure 6.5. Comparison between the time profiles of the 775 CE event (black line) and the 993/994 CE event (red dotted line). These data are the average of the northern hemisphere series from Büntgen et al. (2018).

an extreme SEP event. ^{10}Be increases have been reported around the expected age of 993/994 CE in quasi-annual data from Greenland and Antarctic ice cores (NEEM, NGRIP, and DF). The magnitude of these increases is consistent across ice cores: a $\sim 50\%$ increase in ^{10}Be concentration above baseline (Sigl et al. 2015; Mekhaldi et al. 2015; Miyake et al. 2019). Mekhaldi et al. (2015) used the $^{36}\text{Cl}/^{10}\text{Be}$ ratios in the measured data to estimate that the energy spectrum of the 993/994 CE event was hard, even compared to the 775 CE event. The SEP origin for the 993/994 CE event is consistent with German, Korean, and Irish historical records of low-latitude aurorae from late 992 CE and early 993 CE (Hayakawa et al. 2017a).

660 BCE Event

Park et al. (2017) reported a rapid $\Delta^{14}\text{C}$ increase of $\sim 13\text{‰}$ over six years near 660 BCE through single-year ^{14}C measurements using German oak tree samples. This ^{14}C variation is similar to that of the 775 CE and 993/994 CE events, except for the longer increase time. Although it is difficult to specify the origin of this event using only ^{14}C data, O'Hare et al. (2019) recently found that the origin is consistent with an extreme SEP event by analyzing ^{10}Be and ^{36}Cl concentrations in Greenland ice cores (GRIP and NGRIP). The ratio of ^{36}Cl to ^{10}Be indicates that the energy spectrum of SEPs for 660 BCE must have been very hard, i.e., close to the energy spectrum of SPE 2005 January 20 (GLE #69). The estimated scale of the 660 BCE event has a range between ~ 100 and 200 times larger than that of GLE #69, making it comparable to the other known extreme SEP events of 774–775 CE and 994–995 CE. The 660 BCE event may be thought to occur after a series of strong/extreme SPEs leading to a somewhat longer increase time. The enhanced solar activity around this spike is also consistently inferred with observational reports of candidate aurorae reported in Assyria dating between 679 BCE and 655 BCE (Hayakawa et al. 2019d). The ^{14}C increase was confirmed by only one wood sample; therefore, more accurate ^{14}C profiles using other samples will be required.

3371 BCE Event

Wang et al. (2017) used Chinese tree-ring data to discover a one-year ^{14}C increase of $\sim 10\%$ in 3372–3371 BCE (called the 3371 BCE event). As with the other events mentioned above, a gradual decline after a sharp increase was observed. It is possible that this ^{14}C variation reflects a fourth detected single-year cosmic-ray event, with the strength being ~ 0.6 that for the 775 CE event (Wang et al. 2017). However, no annual ^{14}C data around 3371 BCE using other tree samples have been reported yet. Future verification will be necessary to elucidate the details of the ^{14}C excursion in 3372–3371 BCE.

6.1.4 Summary and Future Applications

Since the discovery of cosmic-ray events in 775 and 993/994 CE using ^{14}C data, similar rapid-increase patterns have been reported for other cosmogenic isotope data sets, such as ^{10}Be in ice cores. Several factors suggest that these cosmic-ray events were caused by extremely strong SEP events. Uncertainty in estimating the scale of the 775 CE event stems mainly from assumptions about SEP energy spectra, but the best estimates are that the event was at least ~ 10 times larger (a more realistic estimate is a factor of 25–50) than any historical recorded SEP event. ^{10}Be and ^{36}Cl data of higher precision will be helpful in resolving these questions about energy spectra.

Short cosmic-ray increase events were confirmed using signals observed across multiple proxies and multiple archive samples. Extending such an approach, cosmic-ray events can potentially be used as globally synchronous, single-year time markers (i.e., isochrones). Cosmic-ray events as wide-range high-precision time markers can potentially be applied to age dating with one-year accuracy within archive samples such as ice cores (Sigl et al. 2015), or in combination with archaeological and geological samples (e.g., volcanic eruption year; Wacker et al. 2014; Oppenheimer et al. 2017; Büntgen et al. 2017; Hakozaiki et al. 2018). If more past cosmic-ray events are discovered in the future, further applications in this direction can be expected.

6.2 Reconstruction of Energy Spectra

FLORIAN MEKHALDI AND RAIMUND MUSCHELER

As detailed in previous sections, cosmogenic radionuclides can be retrieved and measured in a variety of environmental archives on Earth (mainly tree rings and ice cores). Outstanding peaks in their concentration can indicate the occurrence of hostile SEP events hitting Earth. This has been shown with the seminal discoveries of Miyake et al. (2012, 2013) of unprecedented increases in $\Delta^{14}\text{C}$ within annual tree rings from 774–775 CE as well as from 993–994 CE, thereafter confirmed throughout the globe (Büntgen et al. 2018; Güttler et al. 2015; Jull et al. 2014; Usoskin et al. 2013). The existence of peaks has also been shown in the ^{10}Be concentration of the Greenland ice cores NGRIP, NEEM, and Tunu (Mekhaldi et al. 2015; Sigl et al. 2015) as well as in the Antarctic ice cores WAIS (Sigl et al. 2015) and Dome Fuji (Miyake et al. 2015). Using this information, we can gain knowledge on solar storms from the past in such cases when Earth was hit by strong SEP events, which can vary

greatly in both magnitude and spectral hardness. Here, we will review how the energy spectra of the past SEP events discovered in environmental archives can be reconstructed.

The strength of SEP events is traditionally quantified by their fluence above 30 MeV, F_{30} , representing the (integrated over the entire duration of the event) omnidirectional flux of protons with kinetic energy above 30 MeV, per unit area. This quantity, which is important for the implications of the events, cannot, however, characterize the event itself, because, e.g., events with the same F_{30} can have different fluxes of higher-energy protons, which may lead to an ambiguity in the inferred radionuclide production. Accordingly, the full energy spectrum of SEPs should be evaluated, not only the F_{30} fluence (see Section 2.2.3). Some examples of such spectra are shown in Figure 2.8.

6.2.1 The $^{36}\text{Cl}/^{10}\text{Be}$ Ratio

Extreme solar events found in environmental archives are relatively challenging to quantify and reconstruct in terms of their energy spectra, even with the technological means that we can rely upon today. However, it is possible to establish a straightforward qualitative estimate of the past events via the integrated increases in radionuclide concentrations relative to a natural baseline. This natural baseline can be estimated as the average concentration prior to and following the event—in other words, the concentration of radionuclides produced by incoming galactic cosmic rays and distributed during subsequent transport within the climate system. For instance, the event of 774/775 CE was accompanied by an increased concentration in ice-core ^{10}Be by a factor of about 3.4 (Mekhaldi et al. 2015; Sigl et al. 2015). To put this number in perspective, the ^{10}Be concentration measured in ice cores during solar minima (when the solar shielding is weak) typically only displays an increase of the order of 20%. However, translating this increase factor into a fluence spectrum requires knowledge of the spectral shape of the given event. Webber et al. (2007) computed, using the yield-function approach (see Section 4.2), the ^{10}Be and ^{36}Cl yearly production increases for a number of major SEP events between 1956 and 2005.

This gives us an opportunity to relate the measured radionuclide production increase caused by an event to the calculated production increase produced by events from the space era. As an example, it is estimated that GLE #5 of 1956 February 23, the most prominent and the hardest spectrum SEP event observed to date (Section 2.2), would have increased the yearly ^{10}Be global production by 12%, being the largest SEP-related annual amount of ^{10}Be over the past 70 years. As an opposite example, we can refer to the very strong but soft-spectrum event of 1972 August 4 (GLE #24), which was one of the strongest directly observed event in the sense of F_{30} fluence. Nonetheless, it was estimated (Webber et al. 2007) to lead to only a 2.4% increase in the global yearly ^{10}Be production. This highlights the importance of assessing the spectral hardness of the energy spectrum of the past events. As an illustration, by assuming a hard spectrum as per the 1956 event, one would find the F_{30} of the 775 CE event to be $\approx 5 \times 10^{10}$ protons/cm² (Usoskin et al. 2013). By

Table 6.2. Parameters of the Major Observed SEP Events: The Softness of the Spectrum (F_{30}/F_{200} Ratio; Asvestari et al. 2017) and the Relative $^{36}\text{Cl}/^{10}\text{Be}$ Ratios, Based on the Calculated Global Production Increases in ^{36}Cl and ^{10}Be (Webber et al. 2007; Mekhaldi et al. 2015)

SEP Event	F_{30}/F_{200}	$^{36}\text{Cl}/^{10}\text{Be}$ Ratio
1956 February 23	11	1.2
2005 January 20	14	1.5
1989 September 29	41	2.5
2003 October 29	49	3
2000 July 14	79	3.5
1989 October 19	42	3.6
1959 July 10	—	4
1960 November 12	45	4
1972 August 4	488	6
2001 November 4	187	6

Note. The events are sorted by ascending $^{36}\text{Cl}/^{10}\text{Be}$ ratio.

contrast, assuming a soft spectrum as per the 1972 one would give an F_{30} for the 775 CE of about 4×10^{11} protons/cm². The lack of knowledge of the spectral hardness can therefore render an uncertainty in the F_{30} fluence as large as an order of magnitude, which would have important consequences for the assessment of the event’s impact (Thomas et al. 2013). Moreover, the actual increase in ^{10}Be concentration in an ice core may deviate from that in the global production rate, and a realistic transport needs to be modeled (e.g., McCracken 2004; Sukhodolov et al. 2017). Although there is clear statistical evidence that strong GLEs have very hard spectrum (Asvestari et al. 2017), it is crucially important to evaluate the energy spectrum of each event.

Fortunately, we can rely on the additional information that can be provided by ^{36}Cl concentration measurements from ice cores to estimate a likely spectral hardness. As specified in Section 4.2, ^{10}Be and ^{36}Cl have different sensitivities to incoming solar protons at different kinetic energies (Poluianov et al. 2016; Webber et al. 2007). While the peak response of ^{10}Be nuclides appears for solar protons at energies of 100–200 MeV, ^{36}Cl production by solar protons is mainly due to resonances by interactions of protons of 15–25 MeV energy with ^{40}Ar (Webber et al. 2007). This phenomenon leads to an excess in the ^{36}Cl relative production rate in comparison to ^{10}Be for “soft” spectra versus “hard” ones and can thus be regarded as the “isotopic footprint” of radionuclide production by solar energetic protons. This holds particularly true in the instance of soft events that are characterized by high fluxes of protons with energy above ≈ 30 MeV, compared to above ≈ 200 MeV (F_{30}/F_{200} ; see Figure 2.15). Therefore, one can use the $^{36}\text{Cl}/^{10}\text{Be}$ ratio in order to assess the spectral hardness of ancient events. This is best illustrated by sorting major events from the space era by the $^{36}\text{Cl}/^{10}\text{Be}$ ratio that they can induce (see Table 6.2, which presents the relative $^{36}\text{Cl}/^{10}\text{Be}$ ratio, viz. the ratio of the computed global isotope production by an SEP event normalized to the annual production of isotopes by GCRs). The table demonstrates that hard events such as

the 1956 February 23 one (Figure 2.8) with the F_{30}/F_{200} ratio smaller than 20, lead to a $^{36}\text{Cl}/^{10}\text{Be}$ ratio smaller than 2, whereas very soft events ($F_{30}/F_{200} > 100$) result in a $^{36}\text{Cl}/^{10}\text{Be}$ ratio as large as 6.

Therefore, ice cores provide a unique tool to discover traces of past extreme solar storms but also to better assess their energy spectra, which would not be possible by investigating ^{14}C solely from tree rings. The $^{36}\text{Cl}/^{10}\text{Be}$ ratio can be used to attribute modern analogs to past events in terms of spectral hardness. Subsequently, a fluence can be estimated straightforwardly, as shown below. Of course, there exist a number of uncertainties arising from the use of any data measured from environmental archives such as ice cores and from the models applied, but these uncertainties typically do not exceed a factor of 1.5 for the relative ratios shown in Table 6.2. For instance, the ratio measured in ice cores can differ from that for the global production (discussed above), due to known climate influence with a possible involvement of the North Atlantic Oscillation (Muscheler 2000) for Greenlandic ice cores. The loss of gaseous chlorine and also probably ^{36}Cl at low-accumulation sites such as Vostok, in Antarctica, can also alter the $^{36}\text{Cl}/^{10}\text{Be}$ ratio (Delmas et al. 2004); this has to be taken into account.

6.2.2 Application to Historical Events

In the following, we will briefly review how the energy spectra of historical SEP events have been reconstructed by using the three events that have been confirmed in multiple ice cores to date as an example, i.e., 993/994 CE, 774/775 CE, and 660 BCE. The largest and best studied of these events is the one of 774/775 CE, and the related ice-core measurements are shown in Figure 6.6 with the average ^{10}Be concentration from three ice cores (NEEM, NGRIP, and WAIS) as well as the ^{36}Cl concentration from the GRIP ice core between 760 and 810 CE. First, the natural baseline needs to be established, which has been taken here as the average concentration prior to and following the peak at 774/775 CE. This baseline is illustrated with the dashed lines and can be regarded as the average concentration due to GCR at that time period. The data points making up the peaks over this baseline are considered to be the excess production caused by SEPs, as they cannot be explained by “normal” solar modulation. Due to the residence time of ^{10}Be and ^{36}Cl within the stratosphere and subsequent transport (see Section 4.3), it is expected that peaks as observed in ice cores would last for two to three years. As for ^{36}Cl , the lower resolution of the data accounts for the broader increase. The integrated areas between the peaks and the baseline thus represent the total amount of ^{10}Be (red) and ^{36}Cl (blue) that have been deposited (produced) in the aftermath of the event. The resulting low $^{36}\text{Cl}/^{10}\text{Be}$ relative ratio (1.8 ± 0.2) implies that the event(s) was likely characterized by a very hard spectrum—that is, very high fluxes of protons with energy above 200 MeV. Based on the ratio, the spectral hardness of the SEP event of 2005 January 20 (Figure 2.8) provides the closest modern analog. This was also the case for the events of 993/994 CE and 660 CE, both of which also led to a low $^{36}\text{Cl}/^{10}\text{Be}$ relative ratio (2.1 ± 0.4 and 1.4 ± 0.3 , respectively; Mekhaldi et al. 2015; O’Hare et al. 2019).

Using the different peak response energies of ^{36}Cl and ^{10}Be , one can reconstruct the energy spectrum of past extreme SEP events from environmental archives data.

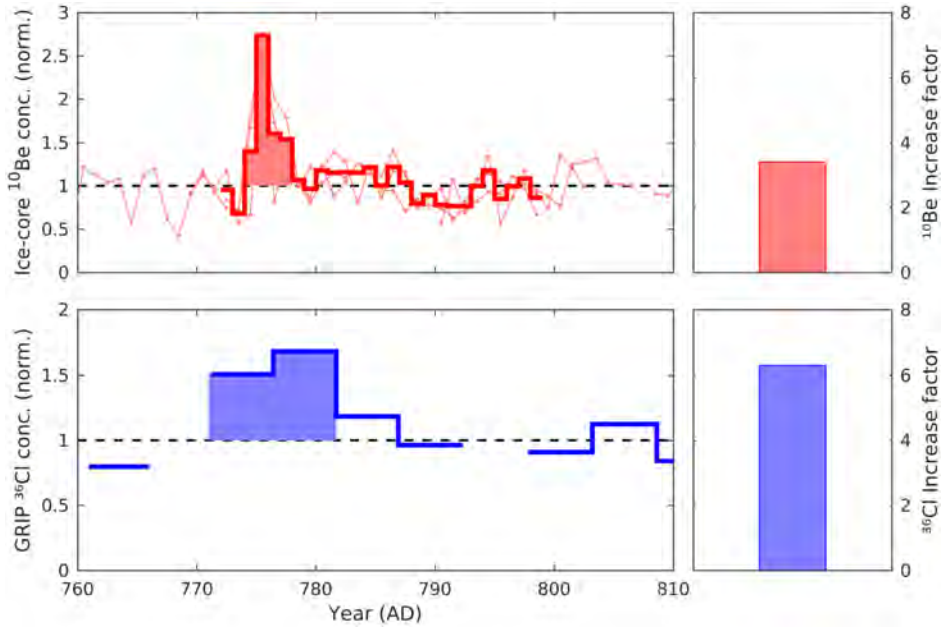


Figure 6.6. The 774/775 CE event as recorded in ice cores. The light red curves in the top panel display the normalized ^{10}Be concentration for the period of 760–810 CE from three ice cores: NGRIP and NEEM from Greenland and WAIS from Antarctica (Mekhaldi et al. 2015; Sigl et al. 2015). The red histogram plot represents a stack of these three normalized records. The dashed black line denotes the natural baseline of the ^{10}Be production by galactic cosmic rays. The filled light red area emphasizes the integrated increase in the concentration caused by the SPE(s) of 774/775 CE. The sum of this area is reported on the right-hand-side panel as the total ^{10}Be increase factor over one year. The bottom panels depict the same but for the normalized ^{36}Cl concentration from the GRIP ice core in central Greenland (Mekhaldi et al. 2015; Wagner et al. 2000).

It can be mentioned here that, because these three events were first discovered in $\Delta^{14}\text{C}$ data from tree-ring records and because ^{14}C , similarly to ^{10}Be , has a peak response energy to solar protons at around 200 MeV (see Section 4.2), it is possible that we are subjected to a detection bias toward hard-spectrum events. Accordingly, some soft-spectrum events with F_{30} reaching 10^{10} protons/cm² may appear, which would be detectable in ^{36}Cl data but not in ice-core ^{10}Be nor tree-ring ^{14}C data.

It is also worth mentioning that the ratio of ^{10}Be to ^{14}C production rates serves as a clear signature of energetic particles versus gamma rays as the source of events (see Sections 4.2.3 and 7.1.1 and Raisbeck et al. 1992; Pavlov et al. 2013).

6.3 Known Visual Auroral Observations

HISASHI HAYAKAWA, EDWARD W. CLIVER, AND YUSUKE EBIHARA

6.3.1 Introduction

The space weather events such as those caused by coronal mass ejections (CMEs) and SEPs have been mostly monitored by instrumental observations; however, the

auroral display provides one of their earliest visual representatives recorded in human history. When interplanetary CMEs (ICMEs) with a southward IMF (interplanetary magnetic field) cause a magnetic storm, the auroral ovals move equatorward in both hemispheres (Gonzalez et al. 1994; Daglis et al. 1999). The major magnetic storms are generally characterized by a great auroral display at mid to low magnetic latitudes, as seen during great magnetic storms such as the Halloween Sequence in 2003 October and the Hydro-Quebec Event in 1989 March (Allen et al. 1989; Daglis 2004).

The aurora is a luminescence phenomenon of molecules and atoms in the upper atmosphere. The bright aurora that can be witnessed by the naked eye is caused by precipitating electrons with energy ranging between ~ 10 eV and $\sim 10^5$ eV. The electrons, which are quasi-stably trapped by Earth's dipolar magnetic field, sometimes precipitate into the upper atmosphere when scattering or acceleration occurs. The scattered electrons are associated with the less-structured diffuse aurora. The origin of the electrons is most likely the plasma sheet in the magnetosphere. During a geomagnetic disturbance, the inner edge of the plasma sheet moves Earthward so that the equatorward boundary of the electron precipitation moves equatorward. The accelerated electrons are associated with the discrete aurora that is structured and are highly variable in space and time. The discrete aurora is embedded in the upward field-aligned current region. During a geomagnetic disturbance, the upward field-aligned current region shifts equatorward, resulting in the equatorward shift of the region of the discrete aurora.

The appearance of aurorae at mid and low latitudes has been associated with the occurrence of sunspots and magnetic disturbances since the early 18th century (e.g., De Mairan 1961; Graham 1724; Hiorter 1747). Later on, Humboldt (1814) and Humboldt & Sabine (1819) monitored the magnetic field for a year and found relatively large magnetic disturbances apart from the diurnal variations; Humboldt named these disturbances “magnetic storms” and found that they are followed by auroral displays. Sabine (1852) associated the trends of magnetic disturbances and aurorae with the trends of sunspot cycles; this association was validated later by more systematic surveys and comparisons of auroral nights and sunspot number from Norwegian observations (Tromholt 1902; Moss & Stauning 2012).

Loomis (1860) is probably one of the earliest who established the idea that aurorae appear frequently along a narrow belt. On the basis of auroral records from 1700 to 1872, Fritz (1881) plotted an occurrence frequency chart of aurorae in the geographic coordinates. The maximum occurrence frequency distribution shows an oval shape, passing through northern Alaska, Canada, and the northernmost part of Europe. This region is called the “auroral zone.” The auroral zone is centered at 67° magnetic latitudes (MLATs) with a latitudinal thickness of 5° – 6° . Feldstein (1960) noticed that the occurrence frequency of overhead aurorae shows a diurnal variation and proposed the concept of the “auroral oval.” The auroral oval is located eccentrically with respect to the geomagnetic pole and is well specified in the magnetic local time (MLT) and magnetic latitude (MLAT) coordinates. The geomagnetic pole is the point at which the dipole magnetic field intersects Earth's surface. The center of the auroral oval is most frequently located at $<65^\circ$ MLAT at

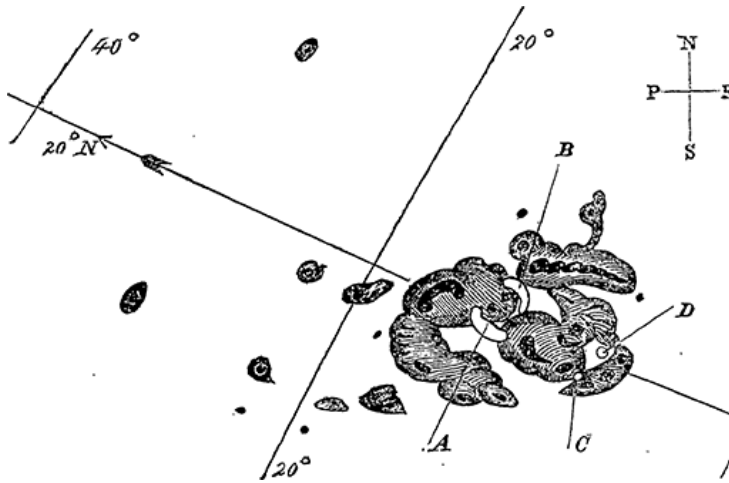


Figure 6.7. A sketch of the sunspots and flares (denoted as A, B, C, and D) on 1859 September 1. Reproduced from Carrington (1859).

midnight (Feldstein 1960). The existence of the auroral oval was confirmed with satellite observations (Anger et al. 1973).

Satellite observations have shown that the auroral oval shifts equatorward in the MLAT–MLT coordinates with increasing geomagnetic activity (Hardy et al. 1985; Carbary 2005). The extension of the auroral oval can be better understood by considering the MLAT, which is defined by the angular distance from the magnetic dipole. The positions of the magnetic poles are reconstructed by multiple archaeomagnetic field models. Among them, the IGRF model is a global standard to compute the drift of the magnetic poles from 1900 to 2019 (Thébault et al. 2015) and has been updated every five years. The GUFM1 model (Jackson et al. 2000) lets us trace the history of the drift of magnetic poles back to 1590. The recent advances in the archaeomagnetic field models allow us to compute the drift of magnetic poles over the last three millennia with Cals3k4b (e.g., Korte & Constable 2011).

6.3.2 Low-latitude Auroral Displays during the Carrington Event in 1859

More direct evidence for the solar–terrestrial relationship was recorded during the 1859 event. Richard Carrington (1859) had monitored a large sunspot group (≈ 2000 – 3000 millionths of the solar hemisphere, μsh) and witnessed a white-light flare in it on 1859 September 1 (Figure 6.7). This was confirmed by a simultaneous observation by Hodgson (1859) and a “magnetic crochet” observed in the magnetograms in the Observatories of Kew and Greenwich (Stewart 1861; Cliver & Svalgaard 2004; Cliver & Keer 2012). About 17.6 hr after this flare, a series of extreme magnetic disturbances, great auroral displays, and resultant telegraph disturbances was observed worldwide (e.g., Tsurutani et al. 2003; Boteler 2006; Green & Boardsen 2006; Nevanlinna 2006, 2008; Cliver & Dietrich 2013; Muller 2014; Lakhina & Tsurutani 2016). The magnetogram at the Colaba Observatory in

Bombay recorded a sharp negative excursion of approximately -1600 nT in the horizontal force (Tsurutani et al. 2003; Cliver & Svalgaard 2004) despite its extremely low magnetic latitude of $\sim 10.3^\circ$. Nevertheless, at that time, there were still some researchers who were not convinced about the relationships between auroral displays and solar activity (e.g., Clark 2007).

During this space weather event, the great auroral displays extended down to low magnetic latitudes (Figure 6.8). These reports were collected in contemporary scientific journals such as the *American Journal of Science*, according to a suggestion by Loomis and his colleagues (Loomis 1859). These reports showed how auroral displays exhibited extreme brightness and extension back then (e.g., Hayakawa et al. 2018c). For example, the auroral display “increased in brilliancy and extent until the whole visible heavens were illuminated; the light at times being such that ordinary print could be read without much difficulty” at Bloomington (Loomis 1859, p. 397). In Chile, “the sky to the south of Santiago was brilliantly illuminated by a light, composed of blue, red, and yellow colors, which remained visible for about three hours,” unlike the monochrome reddish glows that are normally expected in low-latitude aurorae and stable red auroral (SAR) arcs (e.g., Kozyra et al. 1997; Shiokawa et al. 2005). These reports regained scientific attention around the International Geophysical Year (e.g., Chapman 1957b) and were compiled by Kimball (1960). These data were again subjected to consideration especially after the milestone paper by Tsurutani et al. (2003), who characterized this event with an extreme negative excursion of approximately -1600 nT at Colaba Observatory and an extreme extension of auroral visibility of $\sim 22^\circ$ MLAT (Honolulu) in the northern hemisphere and 23° MLAT (Santiago) in the southern hemisphere.

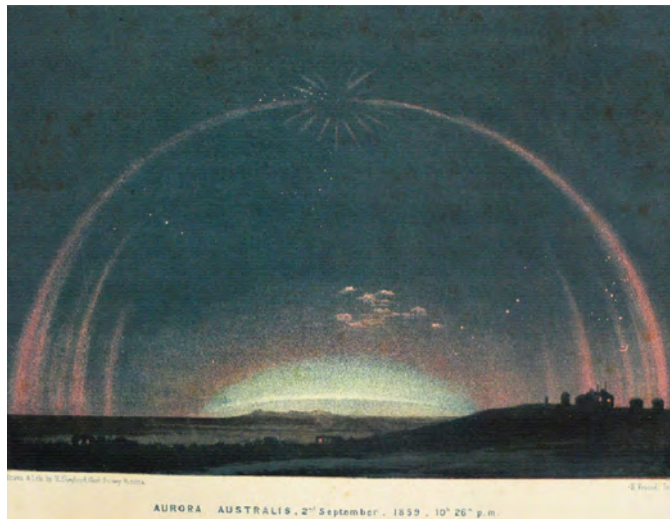


Figure 6.8. A drawing of the auroral display (1859 September 2) as seen from the Flagstaff Observatory (Neumeyer 1863; see also Cliver & Keer 2012).

Auroral records around the Carrington event were surveyed again afterward and subjected to further considerations around the “Workshop on the 1859 ‘Carrington’ Storm” held at the University of Michigan in October 2003. A special issue comprising auroral records in contemporary scientific journals (Shea et al. 2006; Wilson 2006; Silverman 2006), naval logs (Green & Boardsen 2006), and Australian newspapers (Humble 2006) was compiled after the workshop. These surveys were expanded to other historical documents such as Spanish newspapers (Farrona et al. 2011), historical documents and newspapers in Latin America (Moreno Cárdenas et al. 2016; González-Esparza & Cuevas-Cardona 2018), and local treatises and diaries in East Asia (Willis et al. 2007; Hayakawa et al. 2016).

The equatorward boundary of the auroral visibility (22° – 23° MLAT, Tsurutani et al. 2003, versus 18° MLAT, Green & Boardsen 2006) during this event was discussed to consider the possible auroral contribution to the extreme negative excursion observed at the Colaba magnetograms (Green & Boardsen 2006; Cliver & Dietrich 2013; Siscoe et al. 2006). The original records of these reports were comprehensively surveyed (Figure 6.9), and the equatorward boundary of the auroral visibility was reconstructed down to 22.8° MLAT (naval observations) in the northern hemisphere and -21.8° MLAT (Valparaiso) in the southern hemisphere within datable records (Hayakawa et al. 2018c). Note that the report at Honolulu had a slight uncertainty in its dating despite its low-latitude location of 20.5° MLAT, which is even closer to the magnetic equator.

6.3.3 Equatorward Boundary of Auroral Ovals and Storm Intensity

As such, the appearance of an auroral display is considered a visual representation of magnetic storm, as a result of a solar eruption. More importantly, it is empirically known that the equatorward boundary of auroral ovals has a fairly good correlation with the intensity of the magnetic storm. Yokoyama et al. (1998) compared the time series of the equatorward boundary of auroral ovals (magnetic latitude λ) and storm intensity in Dst value for 423 magnetic storms between 1983 and 1991 and plotted them (see Figure 3 in Yokoyama et al. 1998),

$$\text{Dst} \approx -2200 \cdot \cos^6 \lambda + 12 \text{ [nT]}. \quad (6.1)$$

In addition, they compared the time series of the equatorward boundary of auroral ovals and that of the storm intensity (in Dst) during the great magnetic storm on 1989 March 13/14, and plotted them (see Figures 1 and 4 in Yokoyama et al. 1998),

$$\text{Dst} \approx -3400 \cdot \cos^6 \lambda + 60 \text{ [nT]}. \quad (6.2)$$

Nevertheless, we note that we have very little data for auroral displays during the extreme magnetic storms with minimal $\text{Dst} < -300$ nT (Yokoyama et al. 1998). Figure 3 in Yokoyama et al. (1998) shows two data points for auroral events with their equatorward boundary of $\sim 40^{\circ}$ MLAT, ranging from -300 nT to -589 nT. If we apply Equations (6.1) and (6.2) to these cases (equatorward boundary $\sim 40^{\circ}$ MLAT), the values are -433 nT and -627 nT, respectively. Therefore, it is more

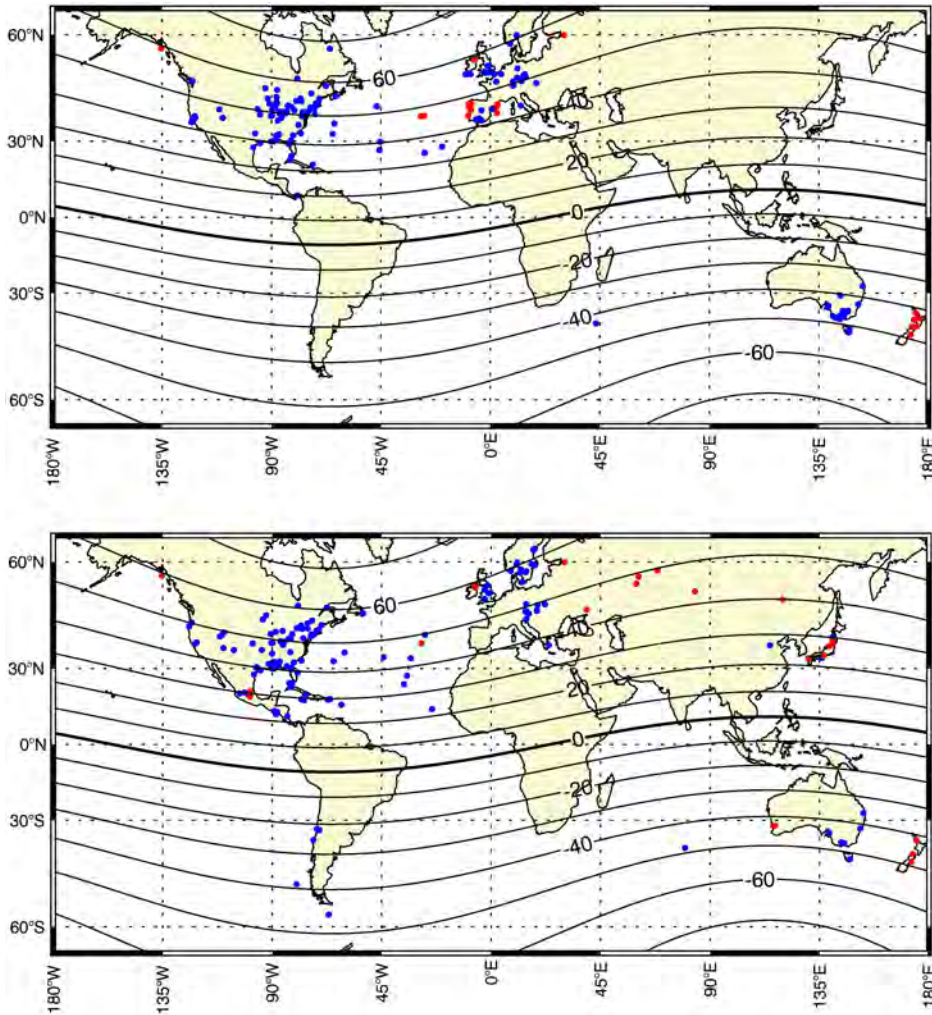


Figure 6.9. Auroral visibility on 1859 August 28/29 and 1859 September 1/2–2/3. The red points show the absolute values for observational sites below 35° MLAT. Reproduced from Hayakawa et al. (2019a). © 2019. The American Geophysical Society. All rights reserved.

conservative to state that the equatorward boundary of the auroral oval has a good correlation with the storm intensity but care should be taken when extrapolating this empirical law beyond the area with enough data.

6.3.4 Reconstruction of the Equatorward Boundary of Auroral Ovals

As such, reconstructing the equatorward boundary of auroral ovals for any specific storms will let us estimate the storm intensity at least relatively. In this context, we should note—even if the auroral display is observed at a given observational site, it does not necessarily mean that the aurora was observed overhead there. For

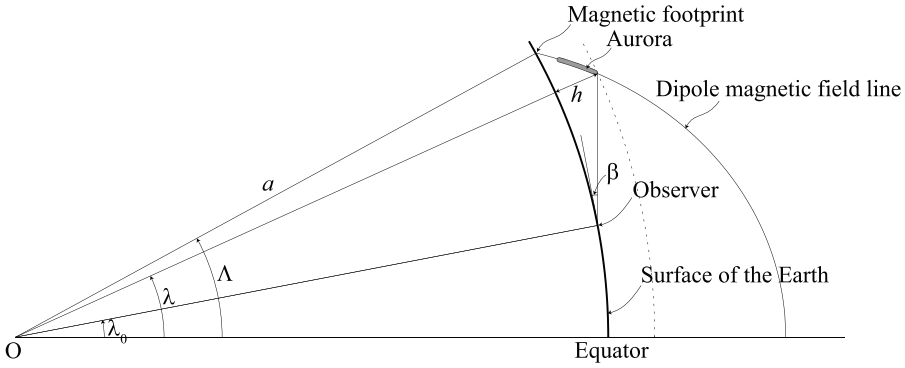


Figure 6.10. Geometry of the magnetic field line and auroral emissions (Hayakawa et al. 2018c). Reproduced from Hayakawa et al. (2018c). © 2018. The American Astronomical Society. All rights reserved.

example, for the 1859 September storm, Kimball (1960, Figure 6 therein) obtained via triangulation an equatorward boundary of overhead aurora of $\sim 35^\circ$ MLAT for the eastern United States versus $\sim 24^\circ$ MLAT for the southern extent of auroral visibility.

As shown in Figure 6.10 (see details in Hayakawa et al. 2018c), the equatorward boundary of auroral ovals (auroral emission regions) is estimated on the basis of the geometry of the dipole magnetic field line, assuming the height of the upper limit of visible auroral emissions and its extension along dipole magnetic field lines and ignoring atmospheric refraction. The magnetic latitude of the equatorward boundary of the aurora oval λ at height h can be estimated with the following equation for a given elevation angle β and MLAT of the observation site λ_0 :

$$(a + h) \cos(\lambda - \lambda_0) = a + (a + h) \sin(\lambda - \lambda_0) \tan \beta. \quad (6.3)$$

Here, a denotes the radius of Earth. With the dipole magnetic field, it is also possible to estimate the magnetic latitude of the magnetic footprint (Λ) of the auroral emissions as follows:

$$\Lambda = \arccos(\cos \lambda (a/(a + h))^{1/2}). \quad (6.4)$$

Λ is referred to as the invariant latitude (ILAT), which is associated with the L -value ($\equiv 1/\cos^2 \Lambda$) as detailed in McIlwain (1961) and Hayakawa et al. (2018c). It is not straightforward to define the auroral height h as the visual auroral height varies with emission wavelength (e.g., Chamberlain 1961). In this section, we use the value of 400 km as the reddish components generally extend from 100 to 400 km in low-latitude aurorae (Roach et al. 1960; Silverman 1998; Ebihara et al. 2017).

6.3.5 Equatorward Boundaries of Auroral Ovals for the Carrington Event

We can reconstruct the equatorward boundary of the auroral oval during the stormy interval around the Carrington event (Hayakawa et al. 2018c). During September 1/2, an aurora was reported at up to 35° in elevation angle in the ship logs of Sabine

(23.1° MLAT), indicating an equatorward boundary of 30.8° ILAT. Estimates based on elevation angle (30°) given in the log books of two other ships (22.8° MLAT) yielded an estimated ILAT for the equatorward boundary of the overhead aurora in this event of 31.3° ILAT. These reports are mostly consistent with the reports of overhead aurora at Mexican cities with MLAT 29°–30° (González-Esparza & Cuevas-Cardona 2018), and they allow us to place the equatorward boundary of the auroral oval in the range 31.8°–32.9° ILAT (Hayakawa et al. 2018c).

The report from Honolulu lets us reconstruct the equatorward boundary of the auroral emission region at ~28.5° ILAT, on the basis of its MLAT of ~20.5° and an elevation angle of ~35°, although, as noted in Hayakawa et al. (2018c), this report has an uncertainty regarding the date.

The Carrington event was preceded by another extreme magnetic storm on August 28/29. At that time, aurora was visible down to Panama (20.2° MLAT), while the elevation angle was not provided in that record (Green & Boardsen 2006; Hayakawa et al. 2018c). Instead, we have a report of an overhead aurora at Havana (34.0° MLAT). If one estimates its height to be 400 km, the magnetic footprint of the auroral display here will be at 36.5° ILAT and will let the observer at Panama see the aurora up to an elevation angle of 7° (Hayakawa et al. 2018c).

6.3.6 Auroral Visibilities during Extreme Space Weather Events

Great Auroral Displays during the Space Age

The largest magnetic storm during the space age, on 1989 August 13/14, had a minimum Dst value of –589 nT (World Data Center for Geomagnetism; see also Cid et al. 2014). It resulted in an over nine-hour shutdown of the electrical grid in Quebec (Allen et al. 1989). Aurorae were reported from the Cayman islands (30.4° MLAT) and from the ship Eland (~29.0° MLAT). There is as yet no consensus regarding the boundary of the overhead aurora (Silverman 2006; Hayakawa et al. 2019a, 2019b), although observations from space by the *DMSP* satellite indicated an equatorward extent of auroral particle precipitation and auroral electric field up to 40.1° MLAT and 35° MLAT, respectively (Allen et al. 1989; Rich & Denig 1992).

The space weather event with the fastest Earthward CME (~2850 km s⁻¹) on 1972 August 4 (Vaisberg & Zastenker 1976; Cliver et al. 1990; Cliver & Svalgaard 2004; Knipp et al. 2018) caused an apparently moderate magnetic disturbance according to its Dst index of approximately –125 nT (Knipp et al. 2018). This failed to be another Carrington event, probably as a consequence of the northward direction of the IMF of this CME (Tsurutani et al. 2003). Visual aurorae were reported from England at ~54° MLAT and from a commercial airline in flight near Bilbao at ~46° MLAT (Taylor & Howarth 1972; McKinnon 1972; Knipp et al. 2018).

The extreme space weather event on 1960 November 13 was considered as one of the most extreme in the ap index, even possibly exceeding that of the Carrington event (Lockwood et al. 2019). During this occasion, aurora was visible down to 35° MLAT (Silverman 2006).

Great Auroral Displays after the Carrington Event

The extreme space weather event on 1882 November 17 is known for the whitish auroral beam seen in the southern sky (Capron 1883). Love (2018) recently examined contemporary magnetograms and reconstructed its value as -386 nT. Silverman (2006) estimated the equatorward boundary of the auroral visibility for this storm as $\sim 37^\circ$ MLAT.

Other storms occurred on 1870 October 24/25, between the Carrington event and another extreme event in 1872 (Vaquero et al. 2008). This event occurred near the peak of solar cycle 11 and is associated with a large sunspot group near the central meridian. The magnetogram at Coimbra captured the magnetic disturbance at -182 nT on October 24 and -281 nT on October 25 in the horizontal force. During this event, auroral displays were reported at Baghdad (28.6° MLAT), Cairo (27.8° MLAT), and Natal (-30.0° MLAT)¹ (see Jones 1955).

Silverman (2006) once compared the equatorward boundary of the auroral visibility (λ_0) with the half-daily *aa* (*A*) index and estimated their relationship as follows:

$$\lambda_0 = 55.86 - 0.56A. \quad (6.5)$$

While this equation may be slightly modified (Table 6.3) because of recent reconstructions, it tells us that the equatorward boundary of visibility may be used to roughly estimate the storm intensity, too, despite the inevitable larger uncertainty caused by the variation of the elevation angle.

6.3.7 Equatorward Boundaries of Outstanding Auroras

Outstanding Aurorae

Despite the extremity of auroral activity around the Carrington event, it does not seem that the Carrington event was exceptional in terms of the equatorward extension of the auroral oval. In the International Geophysical Year, Chapman (1957b) reviewed the history of auroral observations and suggested three more “outstanding auroras” in 1872 February, 1909 September, and 1921 May, comparable to that of 1859 September (see also Hayakawa et al. 2019a). He highlighted the auroral visibility in extremely low MLATs during these storms: Bombay, Singapore, and Samoa. Their magnetic latitude is computed as 10.0° MLAT, -10.0° MLAT, and -16.2° MLAT, respectively, on the basis of archaeomagnetic field models GUFM1 (Jackson et al. 2000) and IGRF12 (Thébault et al. 2015). These extreme extensions of auroral visibility have attracted scientific attention and have been subjected to scientific consideration (Silverman 1995, 2008; Silverman & Cliver 2001; Cliver & Dietrich 2013; Hayakawa et al. 2018b, 2019b). The equatorward boundary of the auroral visibility within 20° from the magnetic equator is certainly intrinsic, and Silverman (2006) suggested the possibility of contribution of

¹ Vaquero et al. (2008) calculated the MLAT for Baghdad, Cairo, and Natal as 26.4° , 23.4° , and -38.5° , respectively. This difference is probably caused by a difference of the archaeomagnetic field model used for calculation.

Table 6.3. Comparison of the Equatorward Boundary of the Auroral Visibility from Ground-based Observations in Absolute Value and the Maximum Half-daily *aa* Value, Revised from Table 1 in Silverman (2006)

Event			Correction		
Year	Month	Date	Maximum Visibility	Maximum Half-daily <i>aa</i>	References
1909	9	25	23 (n.), 30 (s.)	546	Hayakawa et al. (2019b)
1960	11	13	35	462	
1989	3	13	29	452	
1921	5	14	16 (max.), 30 (con.)	441	Hayakawa et al. (2019a)
1872	2	4	10 (max.), 19 (con.)	434	Hayakawa et al. (2018b)
1928	7	7	35	405	This section
1938	1	22	40 (n.), 44 (s.)	383	
1938	1	25	30 (s.), 35 (n.)	350	
1882	11	17	38	348	
1870	10	24/25	28 (s.), 30 (n.)	311	
1892	8	12	46	292	Knipp et al. (2018)
1920	3	22	38	269	
1972	8	4	46	261	
1938	4	16	35	258	
1919	8	11	50	230	
1905	11	15	45	158	
1918	3	7	37	105	
1930	10	17	49	101	
1892	3	9	59	40	
1892	3	21	56	19	
1906	9	17	59	12	
1892	3	22	56	7	
1892	3	23	57	6	

Notes. The equatorward boundary of the auroral visibility for storms are revised according to the references in the last column. For outstanding aurorae, we show the conservative value (con.) and maximum value (max.) for the maximum visibility, as well as its auroral visibility boundary in the northern (n.) and the southern (s.) hemispheres.

sporadic aurorae (e.g., Silverman 2003), especially considering that the equatorward boundary of the auroral visibility did not exceed this line even during the Carrington event.

However, again, note that the auroral visibility in these low-latitude areas does not immediately mean the appearance of overhead aurorae above these observational sites, as shown in Figure 6.10, and hence, they should not necessarily be explained by sporadic aurorae. Therefore, it is important to reconstruct the equatorward boundaries (EBs) of auroral ovals during these events not only to estimate the storm intensity, but also to consider if these reports of low-latitude visibility are indeed realistic.



Figure 6.11. Drawing of an aurora (1872 February 4) from Okazaki, provided by Shounji, with the favor of Mr. Y. Izumi. Reproduced from Hayakawa et al. (2018b). © 2018, The American Astronomical Society. All rights reserved. Note that the Japanese still used the traditional lunisolar calendar back in 1872.

Outstanding Aurorae on 1872 February 4

The first outstanding aurora occurred on 1872 February 4. This storm occurred only one solar cycle after the Carrington event at the local peak during the declining phase of solar cycle 11. During this time interval, aurorae were certainly observed throughout the world with intrinsic magnetic disturbances (Silverman 2008). Apart from the report from Bombay, aurorae were reported from all of Europe, the Caribbean coast, northern India, the Middle East, Northern and Southern Africa, and East Asia with significant brightness, as shown in Figure 6.11 (Silverman 2008; Hayakawa et al. 2018b).

Among these reports, those from Shanghai (19.9° MLAT) and Jacobabad (19.9° MLAT) record overhead aurora extending to the zenith (Chapman 1957a; Hayakawa et al. 2018b). Accordingly, we can reconstruct the equatorward boundary of the auroral oval as up to $\sim 24.2^\circ$ ILAT, and hence, we can expect the observer at Bombay to have seen the aurora at least up to 10° – 15° in elevation angle in the poleward sky, with an assumption of visual auroral height ~ 400 km. The magnetogram at Bombay lets us make a conservative estimate of the negative excursion in the horizontal force as ~ -830 nT (Hayakawa et al. 2018b, 2019a).

Outstanding Aurorae on 1909 September 25

The second outstanding aurora is what was recorded on 1909 September 25. The aurora was reported widely from Europe, Australia, and Japan, and partially from Northern America (Silverman 1995; Hayakawa et al. 2019b). Auroral displays were most significant in East Asia and Australia, where the storm peak fell into the local night. Among these reports, aurorae were reported up to elevation angles of 30° at Matsuyama (23.1° MLAT) in Japan. Accordingly, we can estimate the equatorward boundary of the auroral oval at around $\sim 31.6^\circ$ MLAT (Hayakawa et al. 2019a).

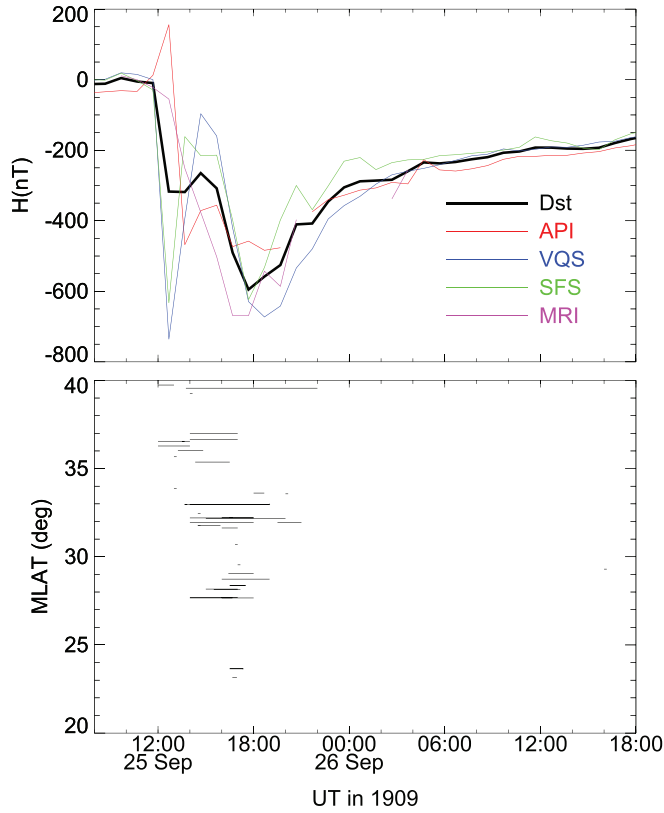


Figure 6.12. Time series of auroral visibility within 40° from the magnetic equator and reconstructed time series of the Dst and horizontal force of four source stations: API (Apia), VQS (Vieques), SFS (San Fernando), and MRI (Mauritius). Reproduced from Hayakawa et al. (2019b), Copyright of OUP Copyright 2019.

This is well explained by the extreme Dst value of -595 nT for this storm (Love et al. 2019a), based on Hayakawa et al. (2019b).

Figure 6.12 shows the time series of auroral visibility within 40° from the magnetic equator and the reconstructed time series of the Dst and horizontal force of four source stations with good chronological agreements (Hayakawa et al. 2019b; Love et al. 2019a). In terms of triangulation, the auroral display should have been above the horizon up to 1.2° and may have been visible from Singapore, while the auroral report from Singapore (-10.0° MLAT) seems possibly rendered from a report of telegraph disturbance (Silverman 1995). Nevertheless, the telegraph disturbance in such low magnetic latitude is already notable, and the time series of the telegraph disturbance shows good agreements with that of low-latitude aurorae.

Outstanding Aurorae on 1921 May 14/15

The third outstanding aurora is that of 1921 May 14/15, based on Hayakawa et al. (2019a). The aurora was mainly visible in the American sector (e.g., Lyman 1921;

Silverman & Cliver 2001). The most equatorward observational site was Apia in Samoa. The MLAT of Samoa is calculated as -16.2° MLAT on the basis of IGRF 12 (Thébault et al. 2015) with a dipole assumption,² and hence, this event is not considered as extreme as the event in Bombay in 1872 (10.0° MLAT) and that in Singapore in 1909 (-10.0° MLAT). Moreover, unlike the other reports in question, this report was described by scientists at the Apia Observatory (Angenheister & Westland 1921).

Angenheister and Westland (Angenheister & Westland 1921, p. 202) described the event as follows: “On May 15d 5-3/4h–6-1/2h, Greenwich (6.15–7 p.m., May 14, local mean time), a display of the aurora australis was observed at this Observatory. There is a range of mountains from 600 to 700 m. high to the south, distant about 10 km; and above this the light could be seen in the form of a segment of a circle, and reaching to an altitude of 22° determined from star positions noted. It covered probably an arc of about 25° along the horizon, and the center was apparently close to the magnetic meridian. In spite of the moonlight (first quarter), and a little twilight as well, the light was very conspicuous and of a glowing red color. The point of the greatest intensity appeared to move from east to west at about 6 h 20 m. Greenwich time, and traces of a brighter yellow colored streamer were noticed at the same time. The sky was quite free from cloud at this hour; later on some small fracto-cumulus were experienced, but no cirrus clouds were seen. No signs of the light were seen after 7 p.m.”

Despite the unfavorable sky brightness with nautical twilight (see also Hayakawa et al. 2019c) and half Moon in its first quarter, the auroral description is quite reasonable, placing its center in the magnetic meridian and showing yellow streamers. As its elevation angle is determined as 22° from star positions, we can reasonably reconstruct the equatorward boundary of the associated auroral oval as $\sim 27.1^\circ$ ILAT (Hayakawa et al. 2019a). This extreme extension of the auroral oval is well confirmed by the reconstructed Dst estimate of approximately -907 ± 132 nT (Hayakawa et al. 2019a; Love et al. 2019b).

6.3.8 Is the Carrington Event Really Exceptional?

As such, the EB of the auroral ovals lets us compare the storm intensity of outstanding aurorae and another extreme event on 1989 March 13/14. Table 6.4 presents a comparison of the equatorward boundary of the auroral oval and Dst value for these storms (Hayakawa et al. 2019a). In terms of auroral extension, the Carrington event only follows other extreme storms on 1872 February 4, and 1921 May 14/15, even if we adopt the report from Honolulu with dating uncertainty. In this sense, the Carrington does not seem exceptional in terms of its spatial auroral evolution.

²Silverman & Cliver (2001) computed its MLAT to be -13.1° based on a corrected geomagnetic model, whereas we compute its MLAT to be -16.2° based on the dipole model (Hayakawa et al. 2019a).

Table 6.4. Comparison of the Equatorward Boundary (EB) of the Auroral Oval and Dst Value of the Outstanding Aurorae and the Hydro-Quebec Event on 1989 March 13/14, Based on Hayakawa et al. (2019a)

Event			EB of Visibility	EB of Oval	Dst Value	References
Year	Month	Date	(MLAT)	(ILAT)	(nT)	
1859	8	28/29	20.2	36.5	$\geq -484^*$	Hayakawa et al. (2018c)
1859	9	1/2	20.5/22.1	28.5/30.8	$\approx -900_{-150}^{+50}^*$	Siscoe et al. (2006), Hayakawa et al. (2018c)
1872	2	4	10.0/18.7	24.2	$< -830^*$	Hayakawa et al. (2018b)
1909	9	25	10.0/23.1	31.6	-595	Hayakawa et al. (2019b), Love et al. (2019a)
1921	5	14/15	16.2	27.1	-907 ± 132	Hayakawa et al. (2019a), Love et al. (2019b)
1989	3	13/14	29	35/40.1	-589	Rich & Denig (1992)

Note. Note that the Dst value indicated by an asterisk (*) shows a preliminary value with single-station data, and the equatorward boundary of the auroral oval for the Hydro-Quebec Event is based on auroral particle precipitation and auroral electric field, captured with the *DMSP* satellite.

This comparison gives us some insights into the Dst value of the Carrington event, too. This Dst value is under discussion and ranges widely from -1760 nT (Tsurutani et al. 2003) as a spot value and -900_{-150}^{+50} nT (Gonzalez et al. 2011; Siscoe et al. 2006; Cliver & Dietrich 2013) as hourly averages, on the basis of observational data. When considering the Dst value, we need to use the hourly average of the horizontal force from four stations by definition to estimate the Dst value (Sugiura 1964). Even though we only have one complete magnetogram from low magnetic latitudes at that time, the definition of the Dst value requires us to use the hourly average of four stations, namely, the value proposed in Siscoe et al. (2006) and Gonzalez et al. (2011).

These auroral records (EB $\sim 28.5^\circ$ ILAT or 30.8° ILAT) seem to favor the hourly average of -900_{-150}^{+50} nT (Gonzalez et al. 2011; Siscoe et al. 2006), which is comparable to the Dst of -907 ± 132 nT versus EB of $\sim 27.1^\circ$ ILAT for the extreme storm on 1921 May 14/15 (Hayakawa et al. 2019b; Love et al. 2019b). Nevertheless, note that these records provide a conservative estimate and can be potentially renewed by new sources from more equatorward observational sites. Moreover, the EB of the auroral oval for the Hydro-Quebec event shows the values of the auroral particle precipitation and auroral electric field, and hence, further reconstruction based on visual auroral records is required to make a sound comparison.

6.3.9 Conclusion

Here, we have reviewed studies of visual auroral reports during known space weather events. First, we reviewed how the aurora is generated during magnetic storms and how its connection with solar activity was understood. Studies of the Carrington event and its consequence showed that low-latitude auroral displays

follow the magnetic storms caused by geo-effective ICMEs with a southward IMF (Gonzalez et al. 1994; Daglis et al. 1999). As the equatorward boundary of auroral ovals have a good empirical correlation with storm intensities (Dst), this boundary can be used as a proxy of intensity of magnetic storms.

As such, it is more important to compute the equatorward boundary of the auroral oval rather than that of the auroral visibility according to the reports on the elevation angle of auroral displays. For the Carrington event, this boundary is reconstructed as 28.5° MLAT (with Honolulu) or 30.8° MLAT (without Honolulu). While this value is certainly extreme, it is not necessarily exceptional in terms of the spatial evolution of the auroral oval in comparison with other outstanding aurorae from 1872 February, 1909 September, and 1921 May (Hayakawa et al. 2019a).

Reconstruction of the equatorward boundary of the auroral oval and Dst index for extreme space weather events is an ongoing effort. Further reconstructions will let us make more stable discussions on the distributions and frequency of such extreme space weather events. Even now, these known data tell us that the Carrington event is probably more frequent and common than a once-in-a-century event (Baker et al. 2008; Riley 2012; Riley & Love 2017; Riley et al. 2018). It is also known that we had a “near miss” of an extreme ICME that may have developed into a Carrington-class magnetic storm, if it had hit the terrestrial magnetic field (Baker et al. 2013; Ngwira et al. 2013; Liu et al. 2014). Further analyses of visual auroral reports will enable us to compare extreme events over a further longer time span.

6.4 Event Statistics and the Worst-case Scenario

EDWARD W. CLIVER AND HISASHI HAYAKAWA

6.4.1 Introduction

What is the largest possible solar flare? In this section, we consider the hierarchy of such events, ranging from the strongest flare ever directly observed, through those inferred from less direct observations such as solar flare effects and cosmogenic nuclides, to the largest flares considered possible over time based on the statistics of observations of SEP events and stellar flares on Sun-like stars. The terrestrial consequences of these extreme events, with emphasis on particle radiation effects, are addressed in Chapter 8.

Before proceeding, we note that the sizes of extreme events, ranging from solar flares to SEP events to geomagnetic storms, are generally uncertain. Such uncertainty arises for two principal reasons:

1. the observed parameter exceeded the dynamic range of the instrument (see, e.g., Figure 5 of Hayakawa et al. 2019b; Love et al. 2019a);
2. the event occurred before the modern era and only indirect observations are available (e.g., Miyake et al. 2012; Hayakawa et al. 2017a, 2017b).

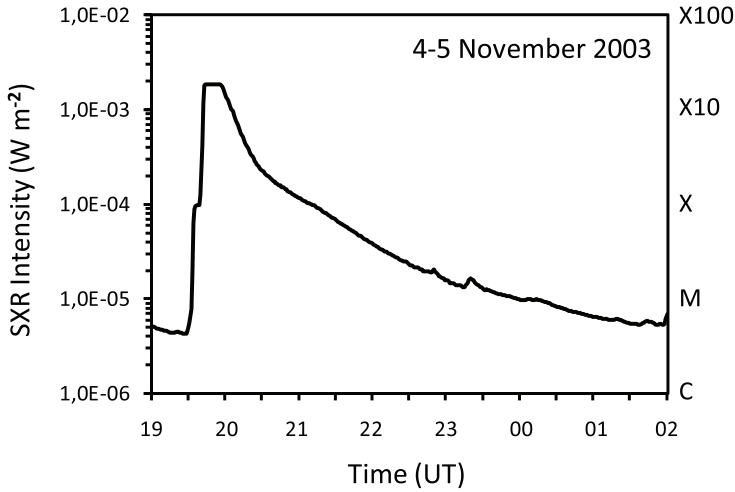


Figure 6.13. The SXR flare observed by *GOES-10* on 2003 November 4–5, the largest solar flare ever directly observed. The 1–8 Å monitor was saturated at a level of 0.00184 W m^{-2} from 19:44–19:56 UT. It is estimated that the flare had an SXR classification of $X35 \pm 5$. The *GOES* SXR flare classification is given on the right-hand axis.

6.4.2 The Hierarchy of Extreme Solar Flares

The Largest Directly Observed Flare

The largest flare that was directly observed is the 2003 November 4 event that occurred during the “Halloween” episode of strong flares in that year (Gopalswamy et al. 2005). For this event, the *GOES* 1–8 Å soft x-ray (SXR) monitor saturated at a level of 0.00184 W m^{-2} for 13 minutes (Figure 6.13). (For the *GOES* SXR classification of flares, see Section 2.1.) Kiplinger & Garcia (2004) used high-time-resolution *GOES* SXR data to infer the unsaturated time profile of this event and obtained a peak classification of X30.6 (0.00306 W m^{-2}). Other estimates of the size of this flare based on sudden ionospheric disturbances (Thomson et al. 2004, 2005; Brodrick et al. 2005) and *Ulysses* >25 keV peak X-ray fluxes (Tranquille et al. 2009) range from $X24.8 \pm 12.6$ to $X45 \pm 5$. Taking these various estimates into account, with preference given to the more direct assessment of Kiplinger & Garcia (2004), Cliver & Dietrich (2013) suggested an SXR class of $X35 \pm 5$ for the 2003 November 4 flare, which had a measured bolometric energy of $\sim 4.3 \times 10^{32} \text{ erg}$ (Emslie et al. 2012), the largest yet directly recorded. Despite the large size of the flare and its favorable (W83) solar location (see Figure 2.18), it did not produce a GLE in neutron monitors.

The Largest Flare Inferred from Electromagnetic Emissions

The next flare in the hierarchy is the largest event inferred from indirect measurements of electromagnetic observations, the well-known Carrington event of 1859 September 1 (the first recorded flare), which was independently observed by Carrington (1859) and Hodgson (1859). A rough estimate of the SXR size of this

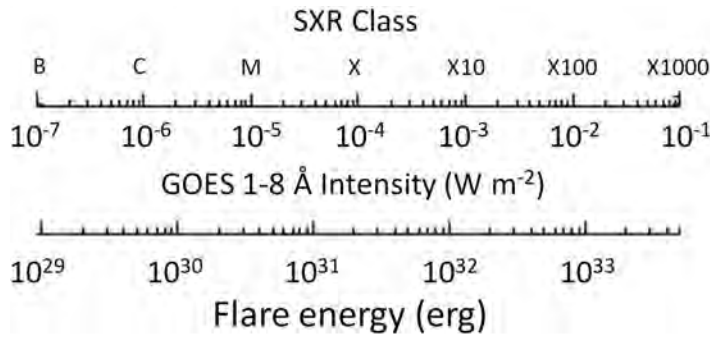


Figure 6.14. Scaling between *GOES* SXR class and flare bolometric energy, adapted from Tschernitz et al. (2018).

flare was obtained by Cliver & Svalgaard (2004) from a comparison of the solar flare effect (SFE; also referred to as the magnetic crochet) of the 1859 flare (Stewart 1861; Bartels 1937) with that of modern crochets for which the SXR class of the associated flare was known.³ Cliver and Svalgaard conservatively concluded that the 1859 flare was an >X10 event. Subsequently, a more sophisticated analysis by Clarke et al. (2010) obtained SXR classifications of X42 and X48 based on magnetograms taken at Greenwich and Kew, respectively. From these values, with reference to Boteler (2006), Cliver & Dietrich (2013) adopted $X45 \pm 5$ as a working value for the size of the 1859 flare. While this flare was associated with a severe magnetic storm and low-latitude aurora (Tsurutani et al. 2003; Cliver & Dietrich 2013; Hayakawa et al. 2018c), it lacked a high-energy SPE (Usoskin & Kovaltsov 2012; Mekhaldi et al. 2019) from analysis of cosmogenic nuclides. Based on the scaling between the flare bolometric energy and SXR class in Figure 6.14, the 1859 flare would have radiated $\sim 4.3 \times 10^{32}$ erg, identical to that directly observed for the 2003 November 4 flare.

The Largest Flare Inferred from Particle Emission

This is a new category, coming into existence only after the discovery of the extremely large 775 CE SEP event in the ^{14}C record (Miyake et al. 2012) that suggested the existence of a commensurate, and therefore huge, flare. At neutron monitor energies (~ 500 MeV), the 775 CE SEP event was a factor of ~ 45 larger than the largest GLE yet observed, the 1956 February 23 event (Meyer et al. 1956). Thus, early guesstimates of the size of the bolometric energy of the flare associated with the 775 CE event were in the 10^{34} erg (Maehara et al. 2015) to 10^{35} erg (Shibata et al. 2013) range. Flares with energies $>10^{33}$ erg, either on the Sun or stars, are termed superflares (Schaefer et al. 2000; Shibata et al. 2013). In the linear scaling of SXR class to radiative energy used by Shibata and Maehara (see Figure 7.14), a flare energy of 10^{34} erg (10^{35} erg) implies an SXR class of X1000 (X10000). Alternatively,

³ An SFE is a type of sudden ionospheric disturbance produced by flare-enhanced conductivity in the E-region of the ionosphere which manifests itself as a sharp feature (that can resemble a crochet hook) on magnetogram traces.

the nonlinear scaling (Figure 6.14) indicates an SXR class \sim X2300 (\sim 40,000) for a 10^{34} erg (10^{35} erg) flare.

Cliver et al. (2014) used a correlation between the logs of the F_{30} SEP fluence and 1–8 Å SXR fluence for a sample of SEP events originating from W20–85 during 1997–2005 and a relationship between the SXR fluence and flare class from Veronig et al. (2002) to obtain an estimate of X230 for the 775 CE event. Based on Figure 6.14, such a flare would have a radiative energy of $\sim 2 \times 10^{33}$ erg, making it a superflare. At present, the X230 ($>2 \times 10^{33}$ erg) estimate is being revisited. Preliminary indications are that the revised estimate will remain in the low end of the superflare range.

The \sim 45-fold enhancement of the intensity of the 775 CE event at GLE energies suggests that, beyond the assumption of a huge solar eruption, special favorable conditions for proton acceleration may apply. One such condition, a pre-event enhancement of background energetic protons in the low corona (Cliver 2006) that can act as seed particles for shock acceleration (e.g., Tylka et al. 2005), was discussed in Section 2.3. Recently, Kong et al. (2017) investigated a possible solar circumstance that bears directly on the acceleration of the high-energy protons. They evaluated the effect of a streamer at the footpoint of the magnetic spiral field line to Earth, which is nominally located at W55 solar longitude. In their simulations, Kong et al. found that when a quasi-perpendicular shock impinged on such a streamer, rather than ambient quiet-Sun field, the acceleration of high-energy protons in the half-GeV range could be significantly enhanced relative to the corresponding effect on protons at >30 MeV energies, as was observed for the 775 CE event (Mekhaldi et al. 2015).

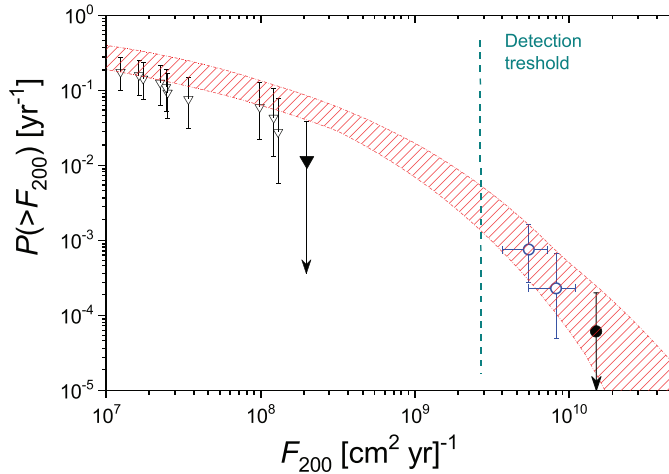


Figure 6.15. Integral probability density function (IPDF) of the occurrence of years with annual >200 MeV fluence (F_{200}) exceeding the given value. The triangles denote data for the space-age era and the blue circles are based on cosmogenic data. Open symbols represent measured/estimated fluences and filled circles are upper limits. Error bars bound the 68% confidence interval. The red hatched area denotes the IPDF for the best-fit Weibull distribution. The green dashed vertical line denotes the current detection threshold for extreme SEP events in cosmogenic data.

Statistics of Extreme Solar Events

Figure 6.15 shows an integral probability density function of the occurrence of years with annual >200 MeV fluences (F_{200}) exceeding the value (in units of 10^9 pr cm^{-2} yr^{-1}) given in the left-hand axis. Triangles refer to space-age data, and circles to cosmogenic-based observations; open circles indicate actual measurements and filled circles conservative upper bounds. The >200 MeV energy is used because it (1) corresponds roughly to the effective energy for the creation of both ^{14}C and ^{10}Be isotopes by SEPs (see Figure 4.35), and (2) is relatively independent of the spectral slope in large SPE events (Kovaltsov et al. 2014). The rightmost circle in Figure 6.15 corresponds to the 775 CE event (Miyake et al. 2012; Mekhaldi et al. 2015; Büntgen et al. 2018; Usoskin et al. 2013), and the open circle to the left of it is based on three smaller events: 993 CE (Miyake et al. 2012; Mekhaldi et al. 2015), ~ 660 BCE (Park et al. 2017; O’Hare et al. 2019), and ~ 3370 BCE (Wang et al. 2017). The gap between the space-age and cosmogenic data may reflect the relative insensitivity of the cosmogenic method (see Section 7.1). Alternatively or in addition, given the hint of a relatively sharp falloff in Figure 6.15 for the space-age data, the gap may reflect a distribution involving different SEP acceleration physics, viz., “normal” events versus the rare occasions when at least one of the special conditions mentioned above occurs in concert with a great (e.g., $>X100$) flare. The figure shows that SEP events as large as the 775 CE event can be expected to occur once every ~ 5000 years. In contrast, flares on Sun-like stars with energies $\sim 10^{33}$ erg, an approximate working value for the 775 CE event, are expected to occur once every ~ 500 – 600 years based on *Kepler* observations (Maehara et al. 2015; see Section 7.3). The longer occurrence interval inferred for a 775 CE-caliber SEP event may reflect the need for additional favorable conditions for SEP acceleration to occur in concert with such a flare.

References

- Allen, J., Frank, L., Sauer, H., & Reiff, P. 1989, *EOSTr*, 70, 1479
- Angenheister, G., & Westland, C. J. 1921, *TeMAE*, 26, 30
- Anger, C. D., Lui, A. T. Y., & Akasofu, S.-I. 1973, *JGR*, 78, 3020
- Asvestari, E., Willamo, T., Gil, A., et al. 2017, *AdSpR*, 60, 781
- Baker, D. N., Balstad, R., Bodeau, J. M., et al. 2008, *Severe Space Weather Events—Understanding Societal and Economic Impacts* (Washington, DC: National Academies Press)
- Baker, D. N., Li, X., Pulkkinen, A., et al. 2013, *SpWea*, 11, 585
- Baroni, M., Bard, E., Petit, J. R., Magand, O., & Boulrès, D. 2011, *GeCoA*, 75, 7132
- Bartels, J. 1937, *TeMAE*, 42, 235
- Boteler, D. H. 2006, *AdSR*, 38, 159
- Brodrick, D., Tingay, S., & Wieringa, M. 2005, *JGR*, 110, A09S36
- Büntgen, U., et al. 2017, *Geo*, 45, 783
- Büntgen, U., Wacker, L., Galván, J. D., et al. 2018, *NatCo*, 9, 3605
- Capron, J. R. 1883, *PMag*, 15, 318
- Carbary, J. F. 2005, *SpWea*, 3, S10001
- Carrington, R. C. 1859, *MNRAS*, 20, 13
- Chamberlain, J. W. 1961, *Physics of the Aurora and Airglow* (New York: Academic)

- Chapman, S. 1957a, *Bull. Nat. Inst. Sci. India*, 9, 180
- Chapman, S. 1957b, *Natur*, 179, 7
- Cid, C., Palacios, J., Saiz, E., Guerrero, A., & Cerrato, Y. 2014, *JSWSC*, 4, A28
- Clark, S. 2007, *The Sun Kings: The Unexpected Tragedy of Richard Carrington and the Tale of How Modern Astronomy Began* (Princeton, NJ: Princeton Univ. Press)
- Clarke, E., Rodger, E., Clilverd, M., et al. 2010, *RAS NAM* 2010, P18
- Cliver, E. W. 2006, *ApJ*, 639, 1206
- Cliver, E. W., & Dietrich, W. F. 2013, *JSWSC*, 3, A31
- Cliver, E. W., Feynman, J., & Garrett, H. B. 1990, *JGR*, 95, 17103
- Cliver, E. W., & Keer, N. C. 2012, *SoPh*, 280, 1
- Cliver, E. W., & Svalgaard, L. 2004, *SoPh*, 224, 407
- Cliver, E. W., Tylka, A. J., Dietrich, W. F., & Ling, A. G. 2014, *ApJ*, 781, 32
- Daglis, I. A. 2004, *Effects of Space Weather on Technology Infrastructure* (Amsterdam: Kluwer)
- Daglis, I. A., Thorne, R. M., Baumjohann, W., & Orsini, S. 1999, *RvGeo*, 37, 407
- De Mairan, J. 1961, *Traite physique et historique de l'Aurora Boreale* (Paris: Academie Royale des Sciences), 1733
- Delmas, R. J., Beer, J., Synal, H.-A., et al. 2004, *TellB*, 56, 492
- Duderstadt, K. A., Dibb, J. E., Schwadron, N. A., et al. 2016, *JGRD*, 121, 2994
- Ebihara, Y., Hayakawa, H., Iwahashi, K., et al. 2017, *SpWea*, 15, 1373
- Eichler, D., & Mordecai, D. 2012, *ApJ*, 761, L27
- Emslie, A. G., Dennis, B. R., Shih, A. Y., et al. 2012, *ApJ*, 759, 71
- Farrona, A. M. M., Gallego, M. C., Vaquero, J. M., & Domínguez-Castro, F. 2011, *Acta Geodaetica et Geophysica Hungarica*, 46, 370
- Feldstein, Y. I. 1960, *Issled. Polyarn. Siyani*, 4, 61
- Fogtman-Schulz, A., Østbø, S. M., Nielsen, S. G. B., et al. 1999, *GeoRL*, 44, 8621
- Fritz, H. 1881, *Das Polarlicht* (Leipzig: Brockhaus)
- Gonzalez, W. D., Echer, E., Tsurutani, B. T., Clúa de Gonzalez, A. L., & Dal Lago, A. 2011, *SSRv*, 158, 69
- Gonzalez, W. D., Joselyn, J. A., Kamide, Y., et al. 1994, *JGR*, 99, 5771
- González-Esparza, J. A., & Cuevas-Cardona, M. C. 2018, *SpWea*, 16, 593
- Gopalswamy, N., Barbieri, L., Cliver, E. W., et al. 2005, *JGRA*, 110, A09S00
- Graham, G. 1724, *RSPT*, 33, 96
- Green, J. L., & Boardsen, S. 2006, *AdSR*, 38, 130
- Güttler, D., Adolphi, F., Beer, J., et al. 2015, *E&PSL*, 411, 290
- Hakozaki, M., Miyake, F., Nakamura, T., et al. 2018, *Radiocarbon*, 60, 261
- Hambaryan, V. V., & Neuhäuser, R. 2013, *MNRAS*, 430, 32
- Hardy, D. A., Gussenhoven, M. S., & Holeman, E. 1985, *JGR*, 90, 4229
- Hayakawa, H., Ebihara, Y., Cliver, E. W., et al. 2019b, *MNRAS*, 484, 4083
- Hayakawa, H., Ebihara, Y., Hand, D. P., et al. 2018c, *ApJ*, 869, 57
- Hayakawa, H., Ebihara, Y., Vaquero, J. M., et al. 2018a, *A&A*, 616, A177
- Hayakawa, H., Ebihara, Y., Willis, D. M., et al. 2018b, *ApJ*, 862, 15
- Hayakawa, H., Ebihara, Y., Willis, D. M., et al. 2019a, *SpWea*, <https://doi.org/10.1029/2019SW002269>
- Hayakawa, H., Iwahashi, K., Tamazawa, H., et al. 2016, *PASJ*, 68, 99
- Hayakawa, H., Mitsuma, Y., Ebihara, Y., & Miyake, F. 2019d, *ApJ*, 884, L18
- Hayakawa, H., Mitsuma, Y., Fujiwara, Y., et al. 2017b, *PASJ*, 69, 17

- Hayakawa, H., Stephenson, F. R., Uchikawa, Y., et al. 2019c, *SoPh*, **294**, 42
- Hayakawa, H., Tamazawa, H., Uchiyama, Y., et al. 2017a, *SoPh*, **292**, 12
- Hiorter, O. 1747, *KSVH*, **8**, 27
- Hodgson, R. 1859, *MNRAS*, **20**, 15
- Hua, Q., & Barbetti, M. 2014, *Radiocarbon*, **46**, 1273
- Humble, J. E. 2006, *AdSR*, **38**, 155
- Humboldt, A. 1814, *Personal Narrative of Travels to the Equinoctial Regions of the New Continent, During the Years 1799-1804* (London: Longman)
- Humboldt, A., & Sabine, E. 1819, *Cosmos: Sketch of a Physical Description of the Universe* (London: Longmans Green)
- Jackson, A., Jonkers, A. R. T., & Walker, M. R. 2000, *RSPTA*, **358**, 957
- Jones, H. S. 1955, *Sunspot and Geomagnetic-Storm Data Derived from Greenwich Observations 1874–1954* (London: HM Stationery Office)
- Jull, A. J. T., Panyushkina, I. P., Lange, T. E., et al. 2014, *GeoRL*, **41**, 3004
- Kimball, D. S. 1960, *A Study of the Aurora of 1859*, Scientific Report No. 6 (Fairbanks: University of Alaska), <http://hdl.handle.net/11122/3607>
- Kiplinger, A. L., & Garcia, H. A. 2004, *BAAS*, **36**, 739
- Knipp, D. J., Fraser, B. J., Shea, M. A., & Smart, D. F. 2018, *SpWea*, **16**, 1635
- Kong, X., Guo, F., Giacalone, J., Li, H., & Chen, Y. 2017, *ApJ*, **851**, 38
- Korte, M., & Constable, C. 2011, *PEPI*, **188**, 247
- Kovaltsov, G. A., Usoskin, I. G., Cliver, E. W., Dietrich, W. F., & Tylka, A. J. 2014, *SoPh*, **289**, 4691
- Kozyra, J. U., Nagy, A. F., & Slater, D. W. 1997, *RvGeo*, **35**, 155
- Lakhina, G. S., & Tsurutani, B. T. 2016, *GSL*, **3**, 5
- Lingenfelter, R. E., & Ramaty, R. 1970, in *Proc. 12th Nobel Symp., Radiocarbon Variations and Absolute Chronology*, ed. I. U. Olsson (Stockholm: Almqvist & Wiksell), 513
- Liu, Y. D., Luhmann, J. G., Kajdič, P., et al. 2014, *NatCo*, **5**, 3481
- Lockwood, M., Bentley, S. N., Owens, M. J., et al. 2019, *SpWea*, **17**, 157
- Loomis, E. 1859, *AmJS*, **29**, 385
- Loomis, E. 1860, *AmJS*, **30**, 79
- Love, J. J. 2018, *SpWea*, **16**, 37
- Love, J. J., Hayakawa, H., & Cliver, E. W. 2019a, *SpWea*, **17**, 37
- Love, J. J., Hayakawa, H., & Cliver, E. W. 2019b, *SpWea*, **17**, 1281
- Lyman, H. 1921, *MWRv*, **49**, 406
- Maehara, H., Shibayama, T., Notsu, Y., et al. 2015, *E&PS*, **67**, 59
- McCracken, K. G., & Beer, J. 2015, *SoPh*, **290**, 3051
- McCracken, K. G. 2004, *JGR*, **109**, A04101
- McCracken, K. G., Dreschhoff, G. A. M., Zeller, E. J., Smart, D. F., & Shea, M. A. 2001, *JGR*, **106**, 21585
- McIlwain, C. E. 1961, *JGR*, **66**, 3681
- McKinnon, J. A. 1972, *NOAA technical memorandum ERL SEL-22* (Boulder, CO: Space Environment Laboratory), <https://hdl.handle.net/2027/uc1.31822031474919>
- Mekhaldi, F., Beer, J., Vockenhuber, C., et al. 2019, *Investigating the Potential to Document Past Solar Storms Using ³⁶Cl in the Greenland Ice Cores NGRIP and Dye-3 for the Past 600 Years Vol. 21* (Geophysical Research Abstracts), EGU2019–16305
- Mekhaldi, F., McConnell, J. R., Adolphi, F., et al. 2017, *JGRD*, **122**, 11900

- Mekhaldi, F., Muscheler, R., Adolphi, F., et al. 2015, [NatCo](#), **6**, 8611
- Melott, A. L., & Thomas, B. C. 2012, [Natur](#), **491**, E1
- Meyer, P., Parker, E. N., & Simpson, J. A. 1956, [PhRv](#), **104**, 768
- Miyake, F., Horiuchi, K., Motizuki, Y., et al. 2019, [GeoRL](#), **46**, 11
- Miyake, F., Masuda, K., Hakozaiki, M., et al. 2014, [Radiocarbon](#), **56**, 1189
- Miyake, F., Masuda, K., & Nakamura, T. 2013, [NatCo](#), **4**, 1748
- Miyake, F., Nagaya, K., Masuda, K., & Nakamura, T. 2012, [Natur](#), **486**, 240
- Miyake, F., Suzuki, A., Masuda, K., et al. 2015, [GeoRL](#), **42**, 84
- Moreno Cárdenas, F., Cristancho Sánchez, S., & Vargas Domínguez, S. 2016, [AdSR](#), **57**, 257
- Moss, K., & Stauning, P. 2012, [HGSS](#), **3**, 53
- Muller, C. 2014, [OLEB](#), **44**, 185
- Muscheler, R. 2000, PhD thesis, ETH Zürich
- Neumeyer, G. 1863, Results of the Meteorological Observations Taken in the Colony of Victoria, During the Years 1859-1862, and of the Nautical Observations Collected and Discussed at the Flagstaff Observatory, Melbourne, During the Years 1858-1862 (Melbourne: Ferres)
- Nevanlinna, H. 2006, [AdSR](#), **38**, 180
- Nevanlinna, H. 2008, [AdSR](#), **42**, 171
- Ngwira, C. M., Pulkkinen, A., Leila Mays, M., et al. 2013, [SpWea](#), **11**, 671
- O'Hare, P., Mekhaldi, F., Adolphi, F., et al. 2019, [PNAS](#), **116**, 5961
- Oppenheimer, C., et al. 2017, [QSRv](#), **158**, 164
- Park, J., Southon, J., Fahrni, S., Creasman, P. P., & Mewaldt, R. 2017, [Radiocarbon](#), **59**, 1147
- Pavlov, A. K., Blinov, A. V., Konstantinov, A. N., et al. 2013, [MNRAS](#), **435**, 2878
- Pedro, J. B., Smith, A. M., Duldig, M. L., et al. 2009, in Advances in Geosciences, Vol. 14, Solar Terrestrial (Singapore: World Scientific), 285
- Poluianov, S. V., Kovaltsov, G. A., Mishev, A. L., & Usoskin, I. G. 2016, [JGRD](#), **121**, 8125
- Raisbeck, G. M., Yiou, F., Jouzel, J., et al. 1992, in Nato ASI Series 1, Global Environmental Change, Vol. 2, The Last Deglaciation: Absolute and Radiocarbon Chronologies (New York: Springer), 127
- Rakowski, A. Z., Krapiec, M., Huels, M., Pawlyta, J., & Boudin, M. 2018, [Radiocarbon](#), **60**, 1249
- Rakowski, Z., Krapiec, M., Huels, M., et al. 2015, [NIMPB](#), **361**, 564
- Reimer, P. J., Bard, E., Bayliss, A., et al. 2013, [Radiocarbon](#), **55**, 1869
- Rich, F. J., & Denig, W. F. 1992, [CaJPh](#), **70**, 510
- Riley, P. 2012, [SpWea](#), **10**, 02012
- Riley, P., Baker, D., Liu, Y. D., et al. 2018, [SSRv](#), **214**, 21
- Riley, P., & Love, J. J. 2017, [SpWea](#), **15**, 53
- Roach, F. E., Moore, J. G., Bruner, E. C. Jr., Cronin, H., & Silverman, S. M. 1960, [JGR](#), **65**, 3575
- Sabine, E. 1852, [RSPT](#), **142**, 103
- Schaefer, B. E., King, J. R., & Deliyannis, C. P. 2000, [ApJ](#), **529**, 1026
- Shea, M. A., Smart, D. F., McCracken, K. G., Dreschhoff, G. A. M., & Spence, H. E. 2006, [AdSR](#), **38**, 232
- Shibata, K., Isobe, H., Hillier, A., et al. 2013, [PASJ](#), **65**, 49
- Shiokawa, K., Ogawa, T., & Kamide, Y. 2005, [JGR](#), **110**, A05202
- Sigl, M., Winstrup, M., McConnell, J. R., et al. 2015, [Natur](#), **523**, 543
- Silverman, S. 1998, [JASTP](#), **60**, 997
- Silverman, S. M. 1995, [JATP](#), **57**, 673

- Silverman, S. M. 2003, [JGR](#), 108, 8011
- Silverman, S. M. 2006, [AdSR](#), 38, 136
- Silverman, S. M. 2008, [JASTP](#), 70, 1301
- Silverman, S. M., & Cliver, E. W. 2001, [JASTP](#), 63, 523
- Siscoe, G., Crooker, N. U., & Clauer, C. R. 2006, [AdSR](#), 38, 173
- Stewart, B. 1861, [RSPT](#), 151, 423
- Stuiver, M., et al. 1998a, [Radiocarbon](#), 40, 1141
- Stuiver, M., Reimer, P. J., & Braziunas, T. F. 1998b, [Radiocarbon](#), 40, 1127
- Suess, H. E. 1955, [Sci](#), 122, 415
- Sugiura, M. 1964, *Ann. Int. Geophys. Year*, 35, 9
- Sukhodolov, T., Usoskin, I. G., Rozanov, E., et al. 2017, [NatSR](#), 7, 45257
- Taylor, M. D., & Howarth, I. 1972, [Astr](#), 9, 83
- Thébault, E., Finlay, C. C., Beggan, C. D., et al. 2015, [E&PS](#), 67, 79
- Thomas, B. C., Melott, A. L., Arkenberg, K. R., & Snyder, B. R. II, 2013, [GeoRL](#), 40, 1237
- Thomson, N. R., Rodger, C. J., & Clilverd, M. A. 2005, [JGR](#), 110, A06306
- Thomson, N. R., Rodger, C. J., & Dowden, R. L. 2004, [GeoRL](#), 31, L06803
- Tranquille, C., Hurley, K., & Hudson, H. S. 2009, [SoPh](#), 258, 141
- Tromholt, S. 1902, *Catalog der in Norwegen bis Juni 1878 beobachteten Nordlichter* (Kristiania: J. Dybwad)
- Tschernitz, J., Veronig, A. M., Thalmann, J. K., Hinterreiter, J., & Ptzi, W. 2018, [ApJ](#), 853, 41
- Tsurutani, B. T., Gonzalez, W. D., Lakhina, G. S., & Alex, S. 2003, [JGR](#), 108, 1268
- Tylka, A. J., Cohen, C. M. S., Dietrich, W. F., et al. 2005, [ApJ](#), 625, 474
- Usoskin, I. G., & Kovaltsov, G. A. 2012, [ApJ](#), 757, 92
- Usoskin, I. G., & Kovaltsov, G. A. 2015, [Icar](#), 260, 475
- Usoskin, I. G., Kromer, B., Ludlow, F., et al. 2013, [A&A](#), 552, L3
- Usoskin, I. G., Solanki, S. K., Kovaltsov, G. A., Beer, J., & Kromer, B. 2006, [GeoRL](#), 33, L08107
- Uusitalo, J., et al. 2018, [NatCo](#), 9, 3495
- Vaisberg, O. L., & Zastenker, G. N. 1976, [SSRv](#), 19, 687
- Vaquero, J. M., Valente, M. A., Trigo, R. M., Ribeiro, P., & Gallego, M. C. 2008, [JGR](#), 113, A08230
- Veronig, A., Temmer, M., Hanslmeier, A., Otruba, W., & Messerotti, M. 2002, [A&A](#), 382, 1070
- Wacker, L., Güttler, D., Goll, J., et al. 2014, [Radiocarbon](#), 56, 573
- Wagner, G., Masarik, J., Beer, J., et al. 2000, [NIMPB](#), 172, 597
- Wang, F. Y., Yu, H., Zou, Y. C., Dai, Z. G., & Cheng, K. S. 2017, [NatCo](#), 8, 1487
- Webber, W. R., Higbie, P. R., & McCracken, K. G. 2007, *JGRA*, 112, A10106
- Willis, D. M., Stephenson, F. R., & Fang, H. 2007, [AnG](#), 25, 417
- Wilson, L. 2006, [AdSR](#), 38, 304
- Wolff, E. W., Bigler, M., Curran, M. A. J., et al. 2012, [GeoRL](#), 39, L08503
- Wolff, E. W., Jones, A. E., Bauguitte, S. J.-B., & Salmon, R. A. 2008, [ACP](#), 8, 5627
- Yokoyama, N., Kamide, Y., & Miyaoka, H. 1998, [AnG](#), 16, 566